

## Mean fields and fluctuations in compressible magnetohydrodynamic flows

James F. Hollins<sup>†</sup>, Graeme R. Sarson<sup>†\*</sup>, Cetin Can Evirgen<sup>†</sup>, Anvar Shukurov<sup>†</sup>, Andrew Fletcher<sup>†</sup> and Fred A. Gent<sup>‡</sup>

<sup>†</sup>School of Mathematics, Statistics and Physics, Newcastle University, Newcastle upon Tyne, NE1 7RU, UK

<sup>‡</sup>Astroinformatics, Department of Computer Science, Aalto University, PO Box 15400, FI-00076, Espoo, Finland

(submitted October 2021)

We apply Gaussian smoothing to obtain mean magnetic field, density, velocity, and magnetic and kinetic energy densities from our numerical model of the interstellar medium, based on three-dimensional magnetohydrodynamic equations in a shearing box  $1 \times 1 \times 2$  kpc in size. The interstellar medium is highly compressible, as the turbulence is transonic or supersonic; it is thus an excellent context in which to explore the use of smoothing to represent physical variables in a compressible medium in terms of their mean and fluctuating parts. Unlike alternative averaging procedures, such as horizontal averaging, Gaussian smoothing retains the three-dimensional structure of the mean fields. Although Gaussian smoothing does not obey the Reynolds rules of averaging, physically meaningful and mathematically sound central statistical moments are defined as suggested by [Germano \(1992\)](#). We discuss methods to identify an optimal smoothing scale  $\ell$  and the effects of this choice on the results. From spectral analysis of the magnetic, density and velocity fields, we find a suitable smoothing length for all three fields, of  $\ell \approx 75$  pc. Such a smoothing scale is likely to be sensitive to the choice of simulation parameters; this may be considered in future work, but here we just explore the methodology. We discuss the properties of third-order statistical moments in fluctuations of kinetic energy density in compressible flows, and suggest their physical interpretation. The mean magnetic field, amplified by a mean-field dynamo, significantly alters the distribution of kinetic energy in space and between scales, reducing the magnitude of kinetic energy at intermediate scales. This intermediate-scale kinetic energy is a useful diagnostic of the importance of SN-driven outflows.

**Keywords:** Magnetohydrodynamics; turbulence; methods: statistical; ISM: kinematics and dynamics; galaxies: ISM

### 1. Introduction

The injection of thermal and kinetic energy by stellar winds and supernova (SN) explosions drives transonic turbulence in the interstellar medium (ISM) and produces an inhomogeneous, multiphase system ([Elmegreen and Scalo 2004](#), [Scalo and Elmegreen 2004](#), [Mac Low and Klessen 2004](#)). The outer scale of turbulent motions in the ISM consistently suggested by observations, theory and simulations is of order 10–100 pc, and the turbulent scales extend to a fraction of a parsec ([Armstrong et al. 1995](#)).

Understanding the properties and nature of a turbulent flow requires the separation of mean and fluctuating quantities. Such a separation is well understood for statistically homogeneous random flows where a number of averaging procedures are available. Volume or area averaging are most important in astronomy, while numerical simulations provide a further opportunity to average over time. Under favourable conditions (defined by ergodic theorems and hypotheses), the resulting averages are equivalent to the statistical ensemble averages employed in theory (e.g., [Monin and Yaglom 2007a](#), [Panchev 1971](#), [Tennekes and Lumley 1972](#)). The ensemble averages are rarely accessible in applications, as their calculation requires the availability of a large number of statistically independent realizations of the random processes.

Space and time averaging procedures are consistent with ensemble averaging  $\langle f + g \rangle = \langle f \rangle + \langle g \rangle$ ,

---

\*Corresponding author. Email: [graeme.sarson@newcastle.ac.uk](mailto:graeme.sarson@newcastle.ac.uk)

$\langle\langle f \rangle\rangle g = \langle f \rangle \langle g \rangle$  and  $\langle\langle f \rangle\rangle = \langle f \rangle$ , where  $f$  and  $g$  are random functions and angular brackets denote averaging (e.g., Sect. 3.1 in [Monin and Yaglom 2007a](#)). Volume and time averaging only satisfy the Reynolds rules in an approximate manner when the scales of variations of the mean quantities and the fluctuations differ significantly (the requirement of scale separation between the averaged quantities and the fluctuations) and the averaging scale is large in comparison with the scale of the fluctuations and small in comparison with that of the mean quantities. In practice, the mean quantities need to be homogeneous or time-independent for the ensemble and volume (or time) averages to be consistent with each other.

The outer scale of the interstellar turbulence is comparable to the scale height of the gas density distribution in spiral galaxies (about 0.1 kpc and 0.5 kpc for the cold and warm diffuse HI, respectively). Therefore, the interstellar turbulent flow cannot be considered statistically homogeneous apart from along the horizontal directions. However, numerical simulations of the supernova-driven, multi-phase ISM have relatively small horizontal domains of order 1 kpc  $\times$  1 kpc or less (e.g., [Korpi et al. 1999](#), [Joung and Mac Low 2006](#), [de Avillez and Breitschwerdt 2007, 2012a,b](#), [Gressel et al. 2008](#), [Federrath et al. 2010](#), [Hill et al. 2012](#), [Gent et al. 2013b,a](#), [Gressel et al. 2013](#), [Bendre et al. 2015](#), [Walch et al. 2015](#), [Girichidis et al. 2016b,a, 2018](#)). Meanwhile, the ISM has a wide range of density and velocity structures (e.g., those related to gas clouds, galactic outflows and spiral patterns) that cover continuously the range of scales from 1 pc to 10 kpc. Therefore, scale separation between the random and large-scale ISM flows is questionable at best. This poses difficulties for the interpretation of numerical simulations. Similar difficulties arise in the interpretation of observations, but numerical simulations have exposed the problems especially clearly.

MHD simulations of galaxies employ domains of scale 10 kpc and larger, and contain kiloparsec-scale structures that would be associated with mean-field dynamics (e.g., [Slyz et al. 2003](#), [Dobbs and Price 2008](#), [Hanasz et al. 2009](#), [Kulesza-Żydzik et al. 2009](#), [Dobbs and Pringle 2010](#), [Pakmor et al. 2016, 2017](#), [Rieder and Teyssier 2016, 2017](#)). Such simulations can also support a small-scale magnetic field driven by dynamo action ([Pakmor et al. 2016, 2017](#), [Rieder and Teyssier 2016, 2017](#)). However, since computational limits restrict the resolution of such simulations to order 10 pc, these simulations are unable to fully model physics such as the injection of SN energy into the ISM and must rely on a simplified prescription. Thus, whilst scale separation may be obtained and lead to useful results for the magnetic field, such results for the velocity field may not be reliable.

Simulations on the scale of interstellar clouds have provided powerful insight into the parsec and sub-parsec physics in the ISM (e.g., [Klessen et al. 2000](#), [Heitsch et al. 2001](#), [Brandenburg et al. 2007](#)). Such simulations drive turbulence at specific wavenumbers to simulate ISM turbulence. Whilst scale separation may be possible, it would be a separation between the parameterised injected flow and any resultant smaller-scale flows. Thus, the results from these scale separations may not be fully informative.

The division of the Navier–Stokes and magnetohydrodynamic (MHD) equations into evolution equations for the mean flow and the fluctuations has been explored for both ensemble averaging and filtering of the fluctuations (also known as coarse-graining); i.e., volume averaging via convolution with a compact kernel. The Reynolds rules of averaging are not satisfied for this procedure but this is not an obstacle to developing a mathematically sound formalism that leads to evolution equations for averaged quantities and their moments ([Germano 1992](#)). The most widely known application of this technique is to subgrid models for large eddy simulations of turbulent flows ([Meneveau 2012](#)). [Eyink \(2018\)](#) and [Aluie \(2017\)](#) provide details and a review of this approach to hydrodynamic and MHD turbulence (see also [Eyink 1995, 2015](#)).

An important advantage of the filtering approach is that, together with ensemble averaging, it does not require scale separation between the mean fields and their fluctuations (e.g., [Aluie 2017](#)). The separation of the mean and fluctuating quantities in a random flow is of crucial significance in the theory of mean-field turbulent dynamos. Mean-field dynamo theory is based on ensemble averaging, but numerical simulations rely on various volume and time averaging procedures. (We note that the algebraic form of the mean-field equations is the same for a wide range of averaging methods:

Germano 1992, Aluie 2017.) For example, the separation of the magnetic field into mean and fluctuating components often involves averaging over the whole computational volume or, in systems stratified along the  $z$ -direction due to gravity, averaging in the  $(x, y)$ -planes (horizontal averaging; see Brandenburg and Subramanian 2005). The resulting mean magnetic field is either perfectly uniform or only dependent on  $z$ . These constraints on the form of the mean magnetic field are often artificial and unphysical. An inhomogeneous system, such as the ISM, is expected to produce a spatially complex mean field, which is ignored by these simple volume or horizontal averaging techniques. A further complication with horizontal averaging, when periodic boundary conditions are used in  $x$  and  $y$ , is that  $\langle B_z \rangle$  must vanish to guarantee the solenoidality of the mean magnetic field (e.g., Gent *et al.* 2013a). The main advantage of horizontal averaging is to obey the Reynolds rules, achieved often at the expense of physical validity. Another, Reynolds rules compliant, option is to use azimuthal averaging in global simulations of dynamo action in a rotating spherical object to obtain an axially symmetric mean magnetic field (see Simard *et al.* 2016, for a review). This approach is easier to justify but still it excludes physically admissible azimuthal variations of the mean field. Furthermore, the kinematic mean-field dynamo action, with homogeneous transport coefficients  $\alpha$  and  $\beta$  (representing the  $\alpha$ -effect and turbulent diffusion), in infinite space produces an inhomogeneous mean magnetic field that varies at all wavenumbers below  $\alpha/\beta$ , with the dominant mode having the wavenumber  $\alpha/(2\beta)$  (e.g., Sokoloff *et al.* 1983). The spatial structure of any mean field is controlled by the physical properties of the system, rather than by the size of the computational domain.

We discuss an alternative approach to averaging based on Gaussian smoothing as suggested by Germano (1992), and employ it to obtain the mean fields in simulations of the multi-phase, supernova-driven ISM. Averaging with a Gaussian (or another) kernel is inherent in astronomical observations, where such smoothing is applied either during data reduction or stems from the finite width of a telescope beam. This approach has been applied by Gent *et al.* (2013a) to the simulated magnetic field; here we extend it to the velocity and density fields and, importantly, energy densities, which represent higher-order statistical moments. In particular, kinetic energy density in a compressible flow represents a third-order statistical moment and requires special attention.

A detailed exploration of the sensitivity of our results to the parameter space is beyond the scope of this paper. Rather, we seek to demonstrate that the extension of this approach to also concern the density and velocity, and thus also kinetic energy, does indeed lead to mathematically and physically meaningful results.

A summary of our numerical model of the ISM is presented in Section 2, and Section 3 introduces averaging based on Gaussian smoothing. Various approaches to the selection of the smoothing length are discussed in Section 4. Section 5 analyses the behaviour of magnetic and kinetic energy densities. Section 6 details the effects of the amplified mean field on the magnetic and kinetic energies. Section 7 compares Gaussian smoothing with horizontal averaging, to show the advantages of the former in the current context. Finally, section 8 summarises and concludes our discussion.

## 2. A numerical model of the multiphase ISM

We use our earlier numerical model of the ISM, described in detail by Gent *et al.* (2013a,b). The model involves solving, with the Pencil Code (Pencil Code Collaboration *et al.* 2021), the full, compressible, non-ideal MHD equations with parameters generally typical of the Solar neighbourhood in a three-dimensional Cartesian, shearing box with radial ( $x$ ) and azimuthal ( $y$ ) extent  $L_x = L_y = 1.024$  kpc and vertical ( $z$ ) extent  $L_z = 1.086$  kpc on either side of the midplane at  $z = 0$ . Our numerical resolution is  $\Delta = \Delta x = \Delta y = \Delta z = 4$  pc, using 256 grid points in  $x$  and  $y$  and 544 in  $z$ . Gent *et al.* (2013a) and, in greater detail, Gent *et al.* (2020) demonstrate that this resolution is sufficient to reproduce the known solutions for expanding SN remnants in the Sedov–Taylor and momentum-conserving phases. Details of the numerical implementation and its comparison with some other similar simulations can be found in Appendix A.

The mass conservation, Navier–Stokes, heat and induction equations are solved for mass density  $\rho$ , velocity  $\mathbf{u}$ , specific entropy  $s$ , and magnetic vector potential  $\mathbf{A}$  (such that  $\mathbf{B} = \nabla \times \mathbf{A}$ ). The Navier–Stokes equation includes a fixed vertical gravity force with contributions from the stellar disc and dark halo. The initial state is an approximate hydrostatic equilibrium. The Galactic differential rotation is modelled by a background shear flow  $\mathbf{U} = (0, -q\Omega x, 0)$ , where  $q$  is the shear parameter and  $\Omega$  is the Galactic angular velocity. Here we use  $q = 1$ , as in a flat rotation curve (i.e., with the rotation speed independent of the cylindrical radius), and  $\Omega = 50 \text{ km s}^{-1} \text{ kpc}^{-1}$ , twice that of the Solar neighbourhood in order to enhance the mean-field dynamo action and thus reduce the computational time. The velocity  $\mathbf{u}$  is the perturbation velocity in the rotating frame, that remains after the subtraction of the background shear flow from the total velocity. However, it still contains a large-scale vertical component due to an outflow driven by the SN activity.

Both Type II and Type I supernova explosions (SNe) are included in the simulations. These differ only in their vertical distribution and frequency. The frequencies used correspond to those in the Solar neighbourhood. We introduce Type II SNe at a mean rate per surface area of  $\nu_{\text{II}} = 25 \text{ kpc}^{-2} \text{ Myr}^{-1}$ . Type I SNe have a mean rate per surface area of  $\nu_{\text{I}} = 4 \text{ kpc}^{-2} \text{ Myr}^{-1}$ . The SN sites have uniform random distribution in the horizontal plane. Their vertical positions have Gaussian distributions with scale heights  $h_{\text{II}} = 0.09 \text{ kpc}$  and  $h_{\text{I}} = 0.325 \text{ kpc}$  for SN II and SN I, respectively.

No spatial clustering of the SNe is included since the size of superbubbles produced by SNe clustering are comparable to the horizontal size of the computational domain. Simulations in a domain of significantly larger size are required to capture the effects of the SN clustering. [de Avillez and Breitschwerdt \(2007\)](#) include SN clustering in their simulations and obtain the correlation scale of the random flows of 75 pc, comparable to those obtained from the correlation analysis of this model (see [Hollins et al. 2017](#)). Each SN is initialised as an injection of  $0.5 \times 10^{51}$  erg of thermal energy and a variable amount of kinetic energy that depends on the local gas density fluctuations and the turbulent ambient velocities, and has the mean net value  $0.4 \times 10^{51}$  erg.

We include optically thin radiative cooling with a parameterised cooling function. For  $T < 10^5 \text{ K}$ , we adopt a power-law fit to the ‘standard equilibrium’ pressure–density curve of [Wolfire et al. \(1995\)](#), as given in [Sánchez-Salcedo et al. \(2002\)](#). For  $T > 10^5 \text{ K}$ , we use the cooling function of [Sarazin and White \(1987\)](#). Photoelectric heating is also included as in [Wolfire et al. \(1995\)](#); it decreases with  $|z|$  on a length scale comparable to the gas scale height near the Sun. The system exhibits distinct hot, warm and cold gas phases identifiable as peaks in the joint probability distribution of the gas density and temperature.

Shock-capturing kinetic, thermal and magnetic diffusivities (in addition to background diffusivities) are included to resolve shock discontinuities and maintain numerical stability in the Navier–Stokes, heat and induction equations. Periodic boundary conditions are used in  $y$ , and sheared-periodic boundary conditions in  $x$ . Open boundary conditions, permitting outflow and inflow, are used at the vertical boundaries at  $z = \pm L_z$ . [Gent et al. \(2013a,b\)](#) provide further details on the boundary conditions used and on the other implementations briefly described above.

Starting with a weak azimuthal magnetic field at the midplane, the system is susceptible to the dynamo instability. Dynamo action can be identified with exponential growth of magnetic field saturating after about 1.4 Gyr at a level of  $2.5 \mu\text{G}$ , comparable to observational estimates for the solar neighbourhood ([Gent et al. 2013a](#)). The magnetic field has energy at a scale comparable to the size of the computational domain, suggesting a mean-field dynamo action ([Gent et al. 2013b](#)).

We analyse snapshots in the range  $0.8 \leq t \leq 1.725 \text{ Gyr}$ . Three distinct temporal stages can be identified in the dynamo action and the magnetic field. With magnetic energy low, compared to the thermal and kinetic energies,  $0.8 \leq t < 1.1 \text{ Gyr}$  hosts the kinematic phase of the mean-field dynamo. The dynamo adjusts itself to a non-linear stage at  $1.1 \leq t < 1.45 \text{ Gyr}$  as the magnetic energy reaches approximate equipartition with kinetic energy of the random flow. Finally, at  $1.45 \leq t \leq 1.725 \text{ Gyr}$ , the mean-field dynamo saturates and the magnetic energy slightly exceeds the kinetic energy (see [Gent et al. 2013b](#)). Since the evolution of the magnetic field is expected to significantly affect the structure of the gas density and velocity, each stage is considered separately. The results are illustrated in the

figures shown below using the snapshot at  $t = 1.6$  Gyr.

### 3. Mean fields and fluctuations in a compressible random flow

Averaging procedures can be used to represent a physical variable  $f$  as a superposition of its mean  $\langle f \rangle$  and fluctuations  $f'$ :  $f = \langle f \rangle + f'$ . Ensemble averaging is used in most theoretical contexts. Ensemble-averaged quantities do not need to be independent of any spatial or temporal variable. However, volume and time averaging are often the only options available in simulations and observations, and those averages clearly are independent of spatial and time variables, respectively. Consider for example, the average over a volume  $V$ ,

$$\langle f \rangle_V = \frac{1}{V} \int_V f(\mathbf{x}') d^3 \mathbf{x}'. \quad (1)$$

It satisfies the Reynolds rules of averaging, including

$$\langle f \langle g \rangle_V \rangle_V = \langle f \rangle_V \langle g \rangle_V, \quad \langle \langle f \rangle_V \rangle_V = \langle f \rangle_V, \quad (2)$$

leading to

$$\langle f' \rangle_V = 0, \quad \langle \langle f \rangle_V g' \rangle_V = 0, \quad (3)$$

for the random variables  $f$  and  $g$ . This allows evolutionary equations for the central moments  $\langle f' g' \rangle_V$ ,  $\langle f' g' h' \rangle_V$  (with another random variable  $h$ ), etc., to be derived by averaging the governing equations using relations, such as for the velocity field  $\mathbf{u}$  (e.g., [Monin and Yaglom 2007a](#)),

$$\begin{aligned} \langle u'_i u'_j \rangle_V &= \langle u_i u_j \rangle_V - \langle u_i \rangle_V \langle u_j \rangle_V, \\ \langle u'_i u'_j u'_k \rangle_V &= \langle u_i u_j u_k \rangle_V - \langle u_i \rangle_V \langle u'_j u'_k \rangle_V - \langle u_j \rangle_V \langle u'_i u'_k \rangle_V - \langle u_k \rangle_V \langle u'_i u'_j \rangle_V - \langle u_i \rangle_V \langle u_j \rangle_V \langle u_k \rangle_V. \end{aligned} \quad (4)$$

In numerical simulations,  $V$  is often the whole computational domain, or some significant part of it, or a (thin) slice parallel to one of the coordinate planes, as in averages over a horizontal plane  $(x, y)$ , or azimuthal averaging. Such averages are constrained to be partially or fully independent of position, in all three directions in the case of volume averages, in two dimensions for horizontal averages and in the azimuth for axial averages. As we discuss in Section 1, these constraints may be, and often are, unreasonably restrictive. Moreover, any observational data obtained with a finite resolution represent a convolution of the quantity observed with the telescope beam, and are free to vary with position. It is therefore desirable to apply to numerical results an averaging procedure, compatible with the observational procedures, in a manner that does not impose unjustifiable restrictions on the averaged quantities. This is the goal of this paper.

A local mean part of a random field  $f(\mathbf{x})$ , denoted  $\langle f \rangle_\ell$ , is obtained by spatial smoothing (filtering) of its fluctuations at scales  $l < \ell$ , with a certain *smoothing length*  $\ell$ , using a smoothing kernel  $\mathcal{G}_\ell$ :

$$\langle f(\mathbf{x}) \rangle_\ell = \int_V f(\mathbf{x}') \mathcal{G}_\ell(\mathbf{x} - \mathbf{x}') d^3 \mathbf{x}', \quad (5)$$

where integration extends over the whole volume where  $f(\mathbf{x})$  is defined. The filtering kernel is normalized, and assumed to be symmetric,

$$\int_V \mathcal{G}_\ell(\mathbf{x} - \mathbf{x}') d^3 \mathbf{x}' = 1, \quad \int_V \mathbf{x} \mathcal{G}_\ell(\mathbf{x}) d^3 \mathbf{x} = 0. \quad (6)$$

To ensure that fluctuations in kinetic energy density are positive definite, the kernel must be positive for all  $\mathbf{x}$  ([Aluie 2017](#), and references therein). The fluctuation field is obtained as

$$f'(\mathbf{x}) = f(\mathbf{x}) - \langle f(\mathbf{x}) \rangle_\ell, \quad (7)$$



(with the link between the prime and the scale  $\ell$  being understood). This procedure retains the spatial structure of both the mean field and the fluctuations. We discuss below physically motivated choices for the smoothing length  $\ell$ .

Thus defined, the averaging procedure does not satisfy the Reynolds rules outlined in equations (2) and (3). In particular, the mean of the fluctuations does not vanish, repeated averaging affects the mean field  $\langle f(\mathbf{x}) \rangle_\ell$ , and the mean and fluctuating fields are not uncorrelated:

$$\langle f' \rangle_\ell \neq 0, \quad \langle \langle f \rangle_\ell \rangle_\ell \neq \langle f \rangle_\ell, \quad \langle \langle f \rangle_\ell f' \rangle_\ell \neq 0. \quad (8)$$

As a consequence, the standard relations between statistical moments of total fields and their fluctuations, shown in equation (4), are no longer valid.

To address these complications, [Germano \(1992\)](#) introduced generalised statistical moments  $\mu(f, g)$ ,  $\mu(f, g, h)$  . . . , of random fields  $f(\mathbf{x})$ ,  $g(\mathbf{x})$  and  $h(\mathbf{x})$  to ensure that the mathematical soundness and simplicity of the averaged governing equations is regained for both the mean fields and their statistical moments. In fact, relations between the statistical moments are quite similar to the standard ones of equation (4). For example, the generalised statistical moments of the velocity field  $\mathbf{u}(\mathbf{x})$  are defined as

$$\begin{aligned} \mu(u_i, u_j) &= \langle u_i u_j \rangle_\ell - \langle u_i \rangle_\ell \langle u_j \rangle_\ell, \\ \mu(u_i, u_j, u_k) &= \langle u_i u_j u_k \rangle_\ell - \langle u_i \rangle_\ell \mu(u_j, u_k) - \langle u_j \rangle_\ell \mu(u_k, u_i) - \langle u_k \rangle_\ell \mu(u_i, u_j) - \langle u_i \rangle_\ell \langle u_j \rangle_\ell \langle u_k \rangle_\ell. \end{aligned} \quad (9)$$

Statistical moments of the fluctuations are obtained from the moments of the total fields and their averages as, for example,

$$\begin{aligned} \langle u'_i u'_j \rangle_\ell &= \langle (u_i - \langle u_i \rangle_\ell)(u_j - \langle u_j \rangle_\ell) \rangle_\ell = \langle u_i u_j - \langle u_i \rangle_\ell u_j - u_i \langle u_j \rangle_\ell + \langle u_i \rangle_\ell \langle u_j \rangle_\ell \rangle_\ell \\ &= \langle u_i u_j - \langle u_i \rangle_\ell u'_j - u'_i \langle u_j \rangle_\ell - \langle u_i \rangle_\ell \langle u_j \rangle_\ell \rangle_\ell \\ &= \langle u_i u_j \rangle_\ell - \langle \langle u_i \rangle_\ell u'_j \rangle_\ell - \langle u'_i \langle u_j \rangle_\ell \rangle_\ell - \langle \langle u_i \rangle_\ell \langle u_j \rangle_\ell \rangle_\ell. \end{aligned} \quad (10)$$

As in equation (8), we have  $\langle \langle u_i \rangle_\ell u'_j \rangle_\ell \neq 0$  and  $\langle u'_i \langle u_j \rangle_\ell \rangle_\ell \neq 0$ . In addition,  $\langle \langle u_i \rangle_\ell \langle u_j \rangle_\ell \rangle_\ell \neq \langle u_i \rangle_\ell \langle u_j \rangle_\ell$  since  $\langle \langle u_i \rangle_\ell \rangle_\ell \neq \langle u_i \rangle_\ell$ . As a consequence,  $\langle u'_i u'_j \rangle_\ell \neq \langle u_i u_j \rangle_\ell - \langle u_i \rangle_\ell \langle u_j \rangle_\ell = \mu(u_i, u_j)$ . Replacing statistical moments of the fluctuations such as  $\langle u'_i u'_j \rangle_\ell$  wherever they appear with generalised central moments such as  $\mu(u_i, u_j)$ , leads to governing equations for the fluctuations in a mathematically simple form practically identical to that obtained under ensemble averaging (see [Aluie 2017](#), for the case of MHD equations). The algebraic structure of the closure is the same, regardless of the choice of the filter  $\mathcal{G}$ . Such a property is called the averaging invariance of the turbulent equations (see [Germano 1992](#)).

In application to the ISM simulations, we consider the decomposition of the physical fields into mean and fluctuating components with the mean fields obtained via filtering with a Gaussian kernel,

$$G_\ell(\mathbf{x}) = (2\pi\ell^2)^{-3/2} \exp\left[-\mathbf{x}^2/(2\ell^2)\right], \quad (11)$$

where  $\ell$  is the smoothing length. We perform this analysis for magnetic field  $\mathbf{B}$ , gas density  $\rho$  and velocity  $\mathbf{u}$ . All averages are denoted with the subscript  $\ell$  and fluctuations with the prime, with the exception of magnetic field fluctuations denoted  $\mathbf{b}$ :

$$\begin{aligned} \mathbf{B} &= \mathbf{B}_\ell + \mathbf{b}, & \mathbf{B}_\ell &= \langle \mathbf{B} \rangle_\ell, & \mathbf{b} &= \mathbf{B} - \mathbf{B}_\ell, \\ \rho &= \rho_\ell + \rho', & \rho_\ell &= \langle \rho \rangle_\ell, & \rho' &= \rho - \rho_\ell, \\ \mathbf{u} &= \mathbf{u}_\ell + \mathbf{u}', & \mathbf{u}_\ell &= \langle \mathbf{u} \rangle_\ell, & \mathbf{u}' &= \mathbf{u} - \mathbf{u}_\ell. \end{aligned} \quad (12)$$

#### 4. The smoothing scale and Fourier spectra

The challenge in applying the filtering approach in our context is to determine an appropriate smoothing length  $\ell$  or its admissible range. We note that the mean and fluctuating parts of different variables,

Table 1. Notation for the total (T), mean (M) and fluctuating (F) fields and their respective Fourier spectra, arising from the filtering decomposition. See section 4 for definitions.

				Spectrum			Energy density			Energy		
	T	M	F	T	M	F	T	M	F	T	M	F
Magnetic field	$\mathbf{B}$	$\mathbf{B}_\ell$	$\mathbf{b}$	$S_B(k)$	$S_{B_\ell}(k)$	$S_b(k)$	$\langle e_B \rangle_\ell$	$e_{B_\ell}$	$e_b$	$\mathcal{E}_B$	$\mathcal{E}_{B_\ell}$	$\mathcal{E}_b$
Gas density	$\rho$	$\rho_\ell$	$\rho'$	$S_\rho(k)$	$S_{\rho_\ell}(k)$	$S_{\rho'}(k)$	—	—	—	—	—	—
Gas velocity	$\mathbf{u}$	$\mathbf{u}_\ell$	$\mathbf{u}'$	$S_u(k)$	$S_{u_\ell}(k)$	$S_{u'}(k)$	$\langle e_k \rangle_\ell$	$e_s$	$e_{st}, e_t$	$\mathcal{E}_k$	$\mathcal{E}_s$	$\mathcal{E}_{st}, \mathcal{E}_t$

e.g.,  $\mathbf{B}$ ,  $\rho$  and  $\mathbf{u}$ , can have different spatial properties and, hence, different smoothing lengths may be required to separate the fluctuations in different variables. For example, [Hollins \*et al.\* \(2017\)](#) find that the correlation lengths of the three variables are different in the simulations discussed here. Unlike applications to subgrid turbulence models, where  $\ell$  is identified with the spatial resolution of a simulation, the choice of  $\ell$  in the present context is motivated by physical considerations. Following [Gent \*et al.\* \(2013b\)](#), we select  $\ell$  using the spectral structure of each variable as discussed below.

Scale separation between the mean and fluctuation fields is required neither by theory based on ensemble averages nor by the filtering technique. Nevertheless, it is natural to expect some difference in scales between the two. For example, the scale of the mean field in a turbulent dynamo is controlled by deviations of the random flow from mirror symmetry and mean velocity shear, whereas turbulent scales depend on the nature of the driving forces. Given the fundamental difference between the two groups of physical effects, it is unlikely that the two parts of magnetic field have similar scales. Since deviations from mirror symmetry are usually weak, the scale of the mean field is expected to be correspondingly large and to exceed the turbulent scale. Arguments of this kind are used to justify the two-scale approach in mean-field magnetohydrodynamics ([Moffatt 1978](#), [Krause and Rädler 1980](#), [Zeldovich \*et al.\* 1983](#)). However, numerical simulations of dynamo systems (including those discussed here) are performed in domains that are only moderately larger than the integral scale of the simulated random flow ([Brandenburg and Subramanian 2005](#), and references therein) which precludes any strong scale separation between the simulated mean and fluctuating fields. Nevertheless, evidence for such separation is usually sought, in the form of a pronounced minimum in the Fourier spectra at a scale exceeding the presumed integral scale of the fluctuations (often, the scale at which the random flow is driven by an explicit force) and the domain size. In application to the magnetic field, [Gent \*et al.\* \(2013b\)](#) demonstrate that the situation can be more subtle and, despite a pronounced difference of the two scales (by a factor of two), the Fourier spectrum of the total magnetic field may not have a noticeable minimum between them.

The Fourier spectrum of the total magnetic field  $\mathbf{B}$  is given by

$$S_B(k) = k^2 \langle |\widehat{\mathbf{B}}(\mathbf{k})|^2 \rangle_k, \quad (13)$$

where  $\widehat{\mathbf{B}}(\mathbf{k}) = \int_V \mathbf{B}(\mathbf{x}) \exp(-2\pi i \mathbf{k} \cdot \mathbf{x}) d^3 \mathbf{x}$  is the Fourier transform of  $\mathbf{B}$  and  $\langle \cdot \rangle_k$  denotes the average value within a spherical shell of thickness  $\delta k$  with radius  $k = |\mathbf{k}|$ . The power spectra for the mean and random fields,  $S_{B_\ell}(k)$  and  $S_b(k)$ , are similarly defined in terms of  $\widehat{\mathbf{B}}_\ell(\mathbf{k})$  and  $\widehat{\mathbf{b}}(\mathbf{k})$ , the Fourier transforms of  $\mathbf{B}_\ell$  and  $\mathbf{b}$ :

$$S_{B_\ell}(k) = k^2 \langle |\widehat{\mathbf{B}}_\ell(\mathbf{k})|^2 \rangle_k, \quad S_b(k) = k^2 \langle |\widehat{\mathbf{b}}(\mathbf{k})|^2 \rangle_k. \quad (14)$$

We also consider the integral scale of each field (Sect. 12.1 in [Monin and Yaglom 2007b](#)),

$$L = \frac{\pi \int_{2\pi/D}^{\pi/\Delta} k^{-1} S(k) dk}{2 \int_{2\pi/D}^{\pi/\Delta} S(k) dk}, \quad (15)$$

calculated using the appropriate power spectrum  $S(k)$ , where  $\Delta$  is the grid spacing and  $D$  the size of the computational domain. Since both the mean field and the fluctuations are inhomogeneous, equation (15) can be used to derive the characteristic scales of both the mean and fluctuating fields: e.g.,  $L_{B_\ell}$  for the mean magnetic field, such that  $L_{B_\ell}^2 \simeq |\mathbf{B}_\ell|/|\nabla^2 \mathbf{B}_\ell|$ . The spectra and lengths scales for  $\rho$ ,  $\mathbf{u}$  and their respective mean and fluctuations are defined in a similar manner and denoted  $S_\rho(k)$ ,

$S_{\rho_\ell}(k)$ ,  $S_{\rho'}(k)$ ,  $S_u(k)$ ,  $S_{u_\ell}(k)$  and  $S_{u'}(k)$ , with the corresponding length scales  $L_\rho$ ,  $L_{\rho_\ell}$ ,  $L_{\rho'}$ ,  $L_u$ ,  $L_{u_\ell}$  and  $L_{u'}$ . The notation is summarized in Table 1.

As discussed in Sections 4.1, 4.2 and 4.3, none of the Fourier spectra of  $\mathbf{B}$ ,  $\rho$  and  $\mathbf{u}$ , have a local minimum. Nonetheless, each variable has distinct, well separated length scales for the mean and fluctuating fields. The optimal smoothing scale  $\ell$  for each variable is obtained under the requirements that: (i) the major maxima in the Fourier spectra of the mean fields and fluctuations in each variable occur on different sides, along the wavenumber axis, of the wavenumber where they intersect; and (ii) that the ratio of the integral scales of the mean fields and the fluctuations is (approximately) maximized.

The power spectrum  $S_B(k)$  is equivalent, up to a constant factor of  $1/(8\pi)$ , to the magnetic energy spectrum  $M(k) = S_B(k)/(8\pi)$ , and the total magnetic energy can be obtained as an integral over the relevant wavenumber range,  $E_B = \int_k M(k) dk$ . However, unlike the case of incompressible flows, the power spectrum of the velocity field cannot be directly equated to the kinetic energy density because of the contribution from the gas density fluctuations.

Calculation of energy densities due to the mean fields and fluctuations should be done with care. To illustrate the general approach, consider magnetic energy. In the filtering approach, the energy densities sum as required from equation (9), with the following definitions:

$$\langle e_B \rangle_\ell = e_{B_\ell} + e_b, \quad e_B = B^2/(8\pi), \quad e_{B_\ell} = B_\ell^2/(8\pi), \quad e_b = \mu(B_i, B_i)/(8\pi) \quad (16)$$

(with summation over repeated indices understood in the final definition). Note that  $e_b \neq b^2/(8\pi)$ ; this is discussed further below. We introduce a distinct notation for the volume integrals of these energy densities, to allow the meaningful summation of the energies:

$$\mathcal{E}_B = \mathcal{E}_{B_\ell} + \mathcal{E}_b, \quad \mathcal{E}_B = \int_V \langle e_B \rangle_\ell dV, \quad \mathcal{E}_{B_\ell} = \int_V e_{B_\ell} dV, \quad \mathcal{E}_b = \int_V e_b dV, \quad (17)$$

where  $dV = d^3\mathbf{x}$ . These energy densities and their volume integrals are summarised in Table 1, and discussed further in section 5.

It is important to appreciate the distinction, within the filtering approach, between the quantities introduced above (which allow a meaningful decomposition of energy), and the ‘naive’ energies obtained directly from the decomposed parts of the field (which differ in some cases, and which do not meaningfully sum). Although energies can be obtained from the latter — via volume integrals of the squared quantities, or via wavenumber integrals of the power spectra — these quantities do not sum to a valid decomposition, and so are not here identified with the energies of the mean and fluctuating parts, or of their sum.

For clarity, we do briefly discuss these alternative definitions of energies here, but we do not include them in Table 1, or use these definitions in the following. The total magnetic energy  $E_B$  satisfies  $E_B = 1/(8\pi) \int_k S_B(k) dk = \int_V e_B dV$  (where  $e_B = B^2/(8\pi)$ , as above); but  $E_B \neq \mathcal{E}_B$ . The integral of the mean field satisfies  $E_{B_\ell} = 1/(8\pi) \int_k S_{B_\ell}(k) dk = \int_V e_{B_\ell} dV$  (where  $e_{B_\ell} = B_\ell^2/(8\pi)$ , as above), and does equate to the mean energy introduced above,  $\bar{E}_{B_\ell} = \mathcal{E}_{B_\ell}$ . But the corresponding quantities for the fluctuating field,  $E_b = 1/(8\pi) \int_k S_b(k) dk = 1/(8\pi) \int_V b^2 dV$ , and  $\mathcal{E}_b = \int_V e_b dV$ , are not equal:  $E_b \neq \mathcal{E}_b$ . As noted above, and discussed in more detail in section 5,  $e_b$  must be defined in terms of the generalised second moment with  $i = j$  (from equation (9)),  $e_b = \mu(B_i, B_i)/(8\pi)$ , so that  $e_b \neq b^2/(8\pi)$ .

To summarise the comparison of energies between the two approaches:  $\mathcal{E}_{B_\ell} = E_{B_\ell}$ , but  $\mathcal{E}_B \neq E_B$ , and  $\mathcal{E}_b \neq E_b$ ; and as noted before, while  $\mathcal{E}_B = \mathcal{E}_{B_\ell} + \mathcal{E}_b$ ,  $E_B \neq E_{B_\ell} + E_b$ . As a result, we focus in the following on the filtered energies ( $\mathcal{E}_B$ , etc.), and do not further refer to the naive energies ( $E_B$ , etc.). We do analyse the Fourier spectra of the basic physical variables in Sections 4.1–4.3 to identify appropriate smoothing lengths  $\ell$ , which can be different for different variables; but then use the filtering approach to derive and discuss the corresponding energy densities in Section 5.



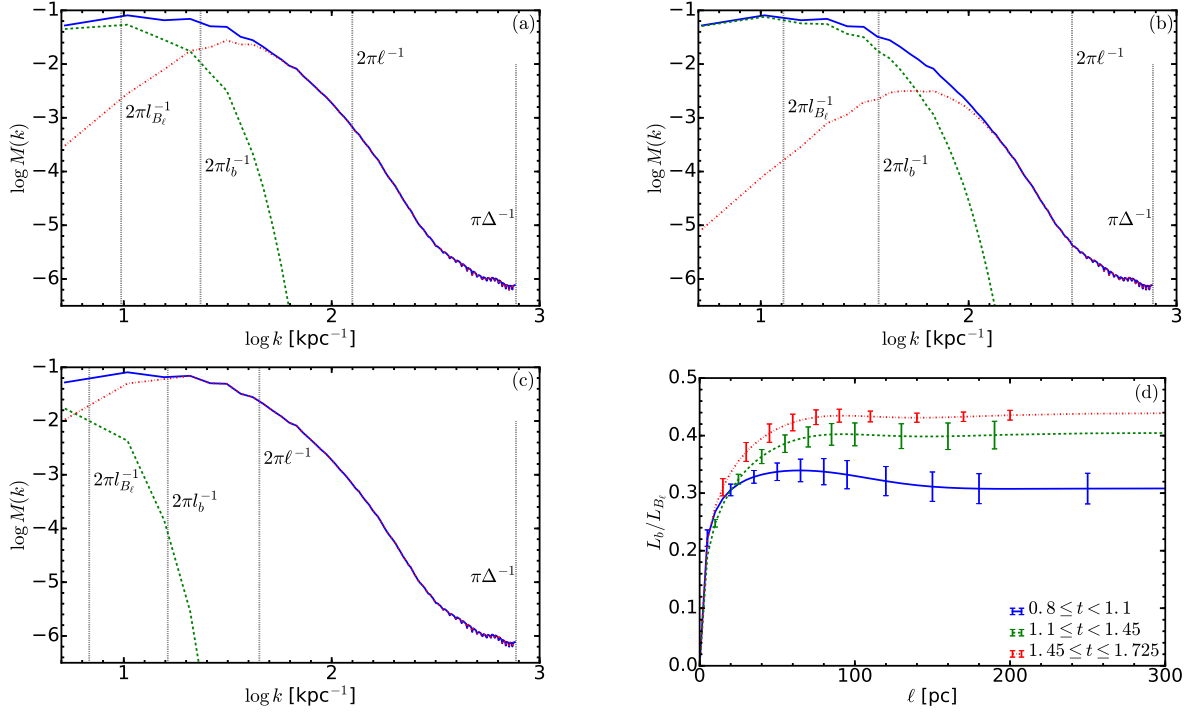


Figure 1. Fourier spectra of the total magnetic field  $S_B(k)$  (solid, blue), its mean part  $S_{B_\ell}(k)$  (dash-dotted, green) and the fluctuations  $S_b(k)$  (dashed, red) for  $\ell = 50$  pc at  $t = 1.6$  Gyr for various values of the smoothing length  $\ell$ : (a)  $\ell = 50$  pc, (b)  $\ell = 20$  pc and (c)  $\ell = 140$  pc. The vertical dotted lines indicate (from left to right) the wavenumbers corresponding to the scale of the mean field  $L_{B_\ell}$ , its fluctuations  $L_b$ , the smoothing length  $\ell$  and the resolution of the simulations  $\Delta$ . (d): Ratio of the integral scales  $L_b$  and  $L_{B_\ell}$  as a function of the smoothing length  $\ell$  in the three stages of magnetic field evolution, kinematic  $0.8 \leq t < 1.1$  Gyr (solid, blue), transitional  $1.1 \leq t < 1.45$  Gyr (dash-dotted, green) and non-linear  $1.45 \leq t \leq 1.725$  Gyr (dashed, red).

#### 4.1. Magnetic field

In figure 1 we show the effect of varying the smoothing length  $\ell$  on the power spectra of the mean magnetic field and its fluctuations. A short  $\ell = 20$  pc (figure 1b) assigns the majority of the energy to the mean field including a large proportion at small scales, while too long  $\ell = 140$  pc (figure 1c) assigns most of the energy to the fluctuations even at very large scales. At wavelength  $\lambda$  the mean and fluctuation power spectra intersect,  $S_{B_\ell}(\lambda) = S_b(\lambda)$ , with  $k > \lambda$  mainly characteristic of fluctuations and  $k < \lambda$  of mean field. We also compute the integral scale  $L$  for the decomposed fields, and would expect  $L_{B_\ell} > \lambda > L_b$ . Instead for  $\ell = 20$  pc,  $\lambda = 0.09$  kpc  $< L_b = 0.17$  kpc, and for  $\ell = 140$  pc  $L_{B_\ell} = 0.92$  kpc  $< \lambda = 1.09$  kpc, which are both physically inconsistent.

A more satisfactory picture emerges when  $\ell = 50$  pc, shown in figure 1a.  $L_{B_\ell} = 0.65$  kpc,  $\lambda = 0.3$  kpc and  $L_b = 0.27$  kpc, such that  $L_b < \lambda < L_{B_\ell}$ . Thus,  $\ell = 50$  pc could be adopted as an appropriate smoothing length for the magnetic field: then the mean field dominates at scales around  $L_{B_\ell}$  whereas the fluctuations contribute most of the power at scales around  $L_b$ .

The ratio of  $L_{B_\ell}$  and  $L_b$  as a function of  $\ell$  is shown in figure 1d for the three stages of the magnetic field evolution. When magnetic field is still weak, there is a pronounced maximum at  $\ell = 65$  pc which becomes less prominent as the magnetic field growth saturates. Thus, the requirement that  $L_b < \lambda < L_{B_\ell}$  is compatible with the maximum scale separation between the mean field and the fluctuations. The ratio reaches an asymptotic value in the range 0.3–0.4 at  $\ell \approx 90$  pc.

#### 4.2. Gas density

Using the same arguments as for magnetic field, we conclude that  $\ell = 50$  pc is a suitable smoothing length for the density distribution, as also shown in figure 2. Indeed, when  $\ell = 50$  pc (figure 2a), we obtain  $L_{\rho_\ell} = 0.62$  kpc  $> \lambda = 0.31$  kpc  $> L_{\rho'} = 0.27$  kpc. In contrast for  $\ell = 20$  pc (figure 2b),

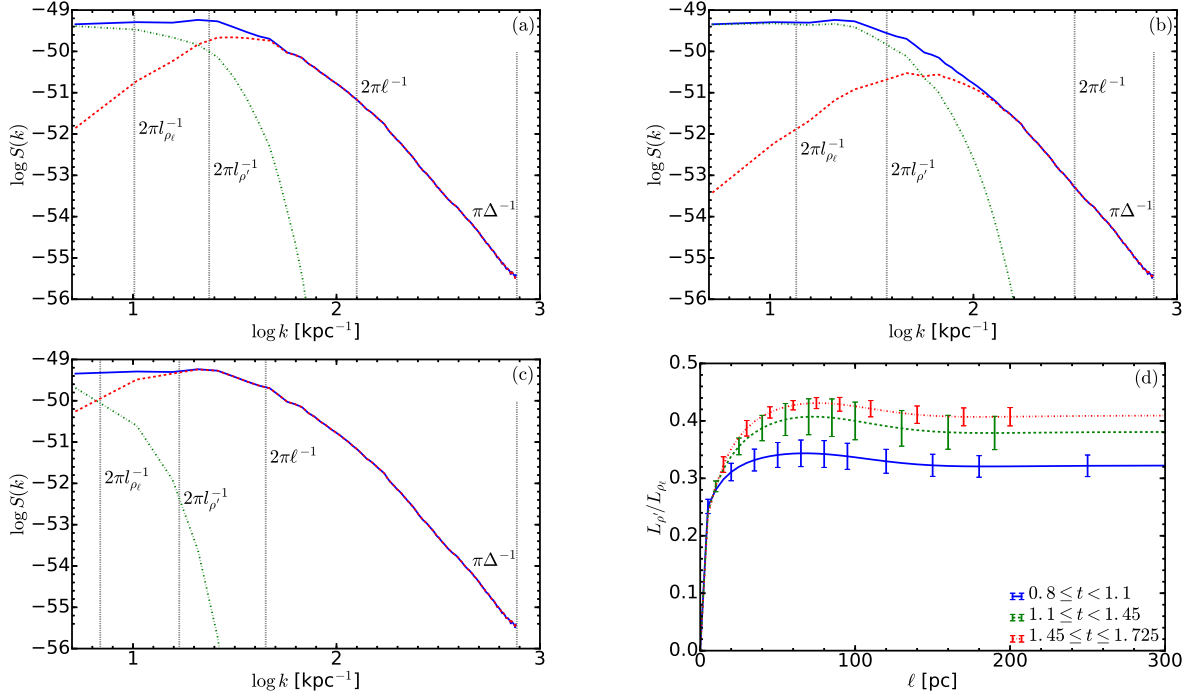


Figure 2. As figure 1 but for the gas density  $\rho$  (in  $\text{g cm}^{-3}$ ) with (a)  $\ell = 50$  pc, (b)  $\ell = 20$  pc and (c)  $\ell = 140$  pc.

$\lambda = 0.11$  kpc  $< L_{\rho'} = 0.17$  kpc and, for  $\ell = 140$  pc (figure 2c),  $L_{\rho_t} = 0.91$  kpc  $< \lambda = 0.95$  kpc. The ratio of  $L_{\rho_t}$  and  $L_{\rho'}$  as a function of  $\ell$  is shown in figure 2d. Its maximum is reached at values of  $\ell$  increasing from 65 pc to 75 pc as the magnetic field saturates, suggesting a suitable smoothing length of approximately 70 pc.

### 4.3. Gas velocity

Figures 3a–d illustrate similar arguments for the velocity field  $\mathbf{u}$  (we recall that  $\mathbf{u}$  represents deviations from the overall shearing flow and contains a systematic vertical outflow velocity). When  $\ell = 50$  pc,  $L_{u_t} = 0.66$  kpc  $> \lambda = 0.3$  kpc  $> L_{u'} = 0.27$  kpc. However, for  $\ell = 20$  pc we have  $\lambda = 0.12$  kpc  $< L_{u'} = 0.16$  kpc, whilst for  $\ell = 140$  pc we have  $L_{u_t} = 0.92$  kpc  $< \lambda = 1.12$  kpc, each in conflict with the demarcations of mean and fluctuation field. Unlike for the magnetic field and gas density spectra, the ratio of length scales in figure 3d does not have any pronounced maxima, as it increases monotonically with  $\ell$  for  $t < 1.45$  Gyr, and has a very broad maximum at  $\ell = 90$ – $100$  pc for  $t > 1.45$  Gyr.

It is clear from each of figures 1, 2 and 3, that the spectral properties of each of these fields are distinct. In addition, the properties of each field vary in time. The simulation times considered here,  $0.8 \leq t \leq 1.725$  Gyr, are all well after the SN-driven hydrodynamics has reached a statistically-steady state, which occurs at about 400 Myr. Thus, we are confident that any changes in time result from the evolution of the mean-field dynamo, which evolves over a time-scale of order Gyr.

It would therefore seem most appropriate to select different smoothing lengths to obtain the fluctuations, depending on both the variable considered and the simulation time. However, complications would then arise with the interpretation of results obtained from such choices. The sensitivity of the results to any change in smoothing length would have to be considered. Theories based on a filtering approach to the MHD equations requires a consistent filter as the averaging operator. Hence, applying different smoothing lengths for each variable would introduce new difficulties when trying to interpret the mean fields and moments of the fluctuating fields as solutions of the filtered equations. In addition, complications could arise when selecting a smoothing scale for moments computed from multiple basic variables, such as the kinetic energy  $\rho \mathbf{u}^2$ . A time dependent smoothing length could be

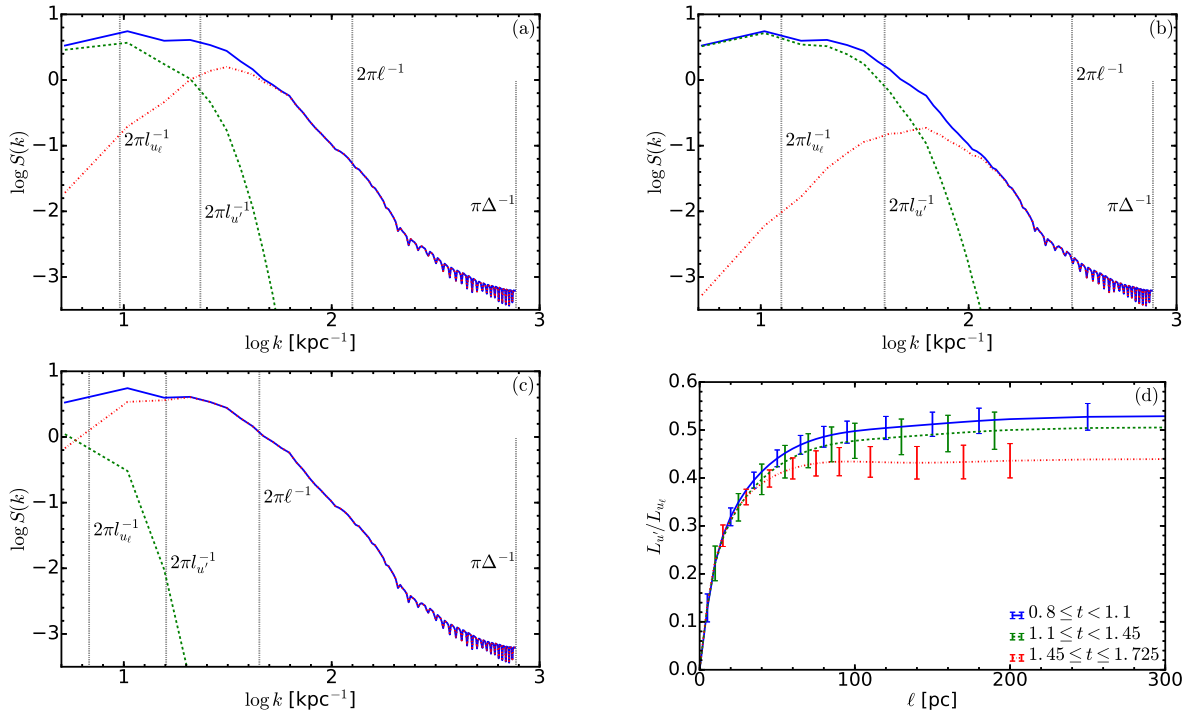


Figure 3. As figure 1 but for the gas velocity (in  $\text{km s}^{-1}$ ) with (a)  $\ell = 50$  pc, (b)  $\ell = 20$  pc and (c)  $\ell = 140$  pc.

used, interpreted as a change in the grid scale of such a simulation.

We suggest it most useful to identify an appropriate value of  $\ell$  that can be used as a smoothing length for all three variables throughout the times considered. We adopt  $\ell = 75$  pc as the smoothing length for magnetic field, gas density and gas velocity, since for magnetic field and gas density the local maxima in the ratios of the mean and fluctuating length scales occur close to 75 pc. For the gas velocity, the value of this ratio at 75 pc is above 90% of the asymptotic value in each stage, whilst the value at 75 pc in the saturated stage is very similar to the value at the broad local maximum.

In the context of the numerical model described in Section 2, this smoothing length is comparable to the correlation scales for the density fluctuations, random velocity and magnetic fields as obtained by Hollins *et al.* (2017). Such a result is sensitive to the choice of simulation parameters. For example, an increased supernova rate results in increased gas compressions, leading to stronger local density gradients and the formation of more filamentary structures. Additionally, stronger local changes in velocity would be observed. Thus, the length scales of the small-scale density and velocity would likely decrease, and so the optimal choice of  $\ell$  would be reduced. Similar effects are likely to be observed with the reduction of the kinematic viscosity and the thermal and magnetic diffusivities.

Such a detailed exploration of the parameter space, involving multiple simulations with different parameter choices, is beyond the scope of this paper. However, in this section, we have successfully demonstrated that an optimal choice of the smoothing length for each of the fundamental physical fields can be reasonably obtained within a detailed simulation of the ISM.

## 5. Energy densities

Magnetic and kinetic energy densities have to be derived using the generalized central moments, as discussed in Section 3. The required moments are derived in Appendix B. Since the mean and fluctuating fields are sensitive to the choice of smoothing length, the resultant energies will also depend on  $\ell$ . The maximum admissible value of  $\ell$  is half the horizontal extent of the simulation domain. We derive the energy densities obtained with various smoothing lengths in the range  $0 < \ell < 0.5$  kpc

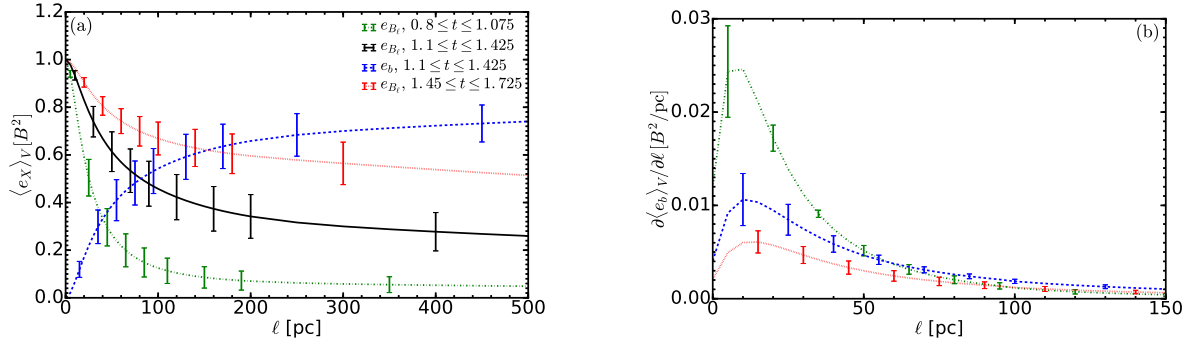


Figure 4. a) Volume averages of the mean magnetic energy density  $\langle e_{B_t} \rangle_V$  at times  $0.8 \leq t < 1.1$  Gyr (green, dash-dotted),  $1.1 \leq t < 1.45$  Gyr (black, solid) and  $t \geq 1.45$  Gyr (red, dotted); also the fluctuating magnetic energy density  $\langle e_b \rangle_V$  at  $1.1 \leq t < 1.45$  Gyr (blue, dashed), as functions of the smoothing length  $\ell$ . These are normalised by the volume average of the smoothed magnetic energy density,  $\langle \langle e_B \rangle_\ell \rangle_V$ , with the volume averaging over the region  $|z| < 0.5$ . b) Derivatives of  $\langle e_b \rangle_V$ , normalised by  $\langle \langle e_B \rangle_\ell \rangle_V$ , with respect to  $\ell$  at  $0.8 \leq t < 1.1$  Gyr (green, dash-dotted),  $1.1 \leq t < 1.45$  Gyr (blue, dashed) and  $t \geq 1.45$  Gyr (red, dotted).

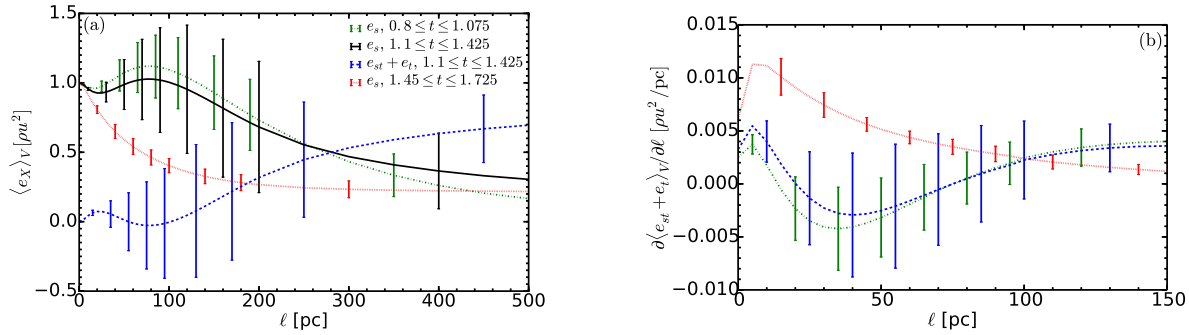


Figure 5. (a) As figure 4a but for the volume average of the mean kinetic energy density  $\langle e_s \rangle_V$  at  $0.8 \leq t < 1.1$  Gyr (green, dash-dotted),  $1.1 \leq t < 1.45$  Gyr (black, solid) and  $t \geq 1.45$  Gyr (red, dotted); with the volume average of the fluctuating kinetic energy density  $\langle e_{st} + e_t \rangle_V$  at  $1.1 \leq t < 1.45$  Gyr (blue, dashed). These are normalised by the volume average of the smoothed kinetic energy  $\langle \langle e_k \rangle_\ell \rangle_V$ . (b) As figure 4b but for the derivative of  $\langle e_{st} + e_t \rangle_V$ , with respect to  $\ell$  (normalised by  $\langle \langle e_k \rangle_\ell \rangle_V$ ); at  $0.8 \leq t < 1.1$  Gyr (green, dash-dotted),  $1.1 \leq t < 1.45$  Gyr (blue, dashed) and  $t \geq 1.45$  Gyr (red, dotted).

and discuss the results in this section. As previously, we consider the three stages of the mean-field dynamo separately, and present results averaged over the snapshots within each stage.

### 5.1. Magnetic energy

The total magnetic energy density is given by

$$e_B = |\mathbf{B}|^2 / (8\pi),$$

with the energy density of the fluctuating magnetic field obtained as

$$e_b = \frac{1}{8\pi} \int_V |\mathbf{B}(\mathbf{x}') - \mathbf{B}_\ell(\mathbf{x})|^2 G_\ell(\mathbf{x} - \mathbf{x}') d^3 \mathbf{x}'. \quad (18)$$

This ensures the energies of the mean and fluctuating magnetic fields sum to the energy of the (filtered) total magnetic energy, i.e.

$$\langle e_B \rangle_\ell = e_{B_\ell} + e_b,$$

where  $e_{B_\ell} = |\mathbf{B}_\ell|^2 / (8\pi)$  is the energy density of the mean magnetic field. We note that  $e_b \neq |\mathbf{b}|^2 / (8\pi)$ , but it can be shown, by expanding  $\mathbf{B}(\mathbf{x}')$  in a Taylor series around  $\mathbf{x}$ , that  $e_b = |\mathbf{b}|^2 / (8\pi) + \mathcal{O}(\ell^2 / L_{B_\ell}^2)$ . Thus, the difference between the volume and filtering averages decreases as  $\ell / L_{B_\ell} \rightarrow 0$ . This fact, also true for any other variable, suggests one consideration for the choice of  $\ell$  might be to maximise the ratio for  $L_{B_\ell} / \ell$ . In practice, however, this would simply lead to  $\ell \rightarrow 0$ ; i.e. all the signal in the mean field, and effectively no decomposition.

The larger is  $\ell$ , the smaller part of the total field is deemed to be a mean field, and  $\langle e_{B_\ell} \rangle_V$  monotonically decreases with  $\ell$  whilst  $e_b$  monotonically increases, as shown in figure 4a. The rate of variation of  $\langle e_b \rangle_V / \langle \langle e_B \rangle_\ell \rangle_V$  with  $\ell$ , shown in figure 4b — and also of  $\langle e_B \rangle_V / \langle \langle e_B \rangle_\ell \rangle_V$ , not shown — becomes relatively small when  $\ell > 50$  pc. This confirms that the appropriate choice for the smoothing length is  $\ell > 50$  pc. (The difference between figure 4a and figure 2a of [Gent \*et al.\* \(2013a\)](#) is caused by a downsampling to a grid  $\Delta x = 8$  pc used in the Fourier transform for that calculation in [Gent \*et al.\* \(2013a\)](#).)

The mean magnetic energy grows with time due to dynamo action, and the value of  $\ell$  for which the two energies are equal to each other increases. At late times, the mean magnetic field is energetically dominant over the fluctuating magnetic field for all  $\ell$ .

## 5.2. Kinetic Energy

In a compressible flow, the mean kinetic energy density is represented by a third-order moment involving the density and velocity fields. Under ensemble (or volume) averaging, the mean kinetic energy density is conveniently — and physically meaningfully — represented (see Section 6.4 in [Monin and Yaglom 2007a](#)) as

$$\begin{aligned} \langle e_k \rangle &= \frac{1}{2} \langle \rho u_i u_i \rangle \\ &= \frac{1}{2} \langle \rho \rangle \langle u_i \rangle \langle u_i \rangle + \langle u_i \rangle \langle \rho' u_i' \rangle + \frac{1}{2} \langle \rho u_i' u_i' \rangle \\ &\equiv e_s + e_{st} + e_t, \end{aligned} \quad (19)$$

where  $e_s$  is the energy density of the mean flow,  $e_t$  is the energy density of the fluctuations and  $e_{st}$  represents the transport of momentum  $\langle \rho' u_i' \rangle$  by the mean flow (summation over repeated indices is understood here and below). An equivalent decomposition is appropriate under the filtering approach as well:

$$\begin{aligned} \langle e_k \rangle_\ell &= \frac{1}{2} \langle \rho u_i u_i \rangle_\ell = e_s + e_{st} + e_t, \\ e_s &= \frac{1}{2} \langle \rho \rangle_\ell \langle u_i \rangle_\ell \langle u_i \rangle_\ell, \\ e_{st} &= \langle u_i \rangle_\ell \mu(\rho, u_i), \\ e_t &= \langle e_k \rangle_\ell - e_s - e_{st} = \frac{1}{2} \langle \rho \rangle_\ell \mu(u_i, u_i) + \frac{1}{2} \mu(\rho, u_i, u_i), \end{aligned} \quad (20)$$

where the moments involved are derived in Appendix B in explicit integral forms:

$$\begin{aligned} e_{st} &= \int_V \mathbf{u}(\mathbf{x}') G_\ell(\mathbf{x} - \mathbf{x}') d^3 \mathbf{x}' \int_V \Delta \rho_\ell(\mathbf{x}, \mathbf{x}') \Delta \mathbf{u}_\ell(\mathbf{x}, \mathbf{x}') G_\ell(\mathbf{x} - \mathbf{x}') d^3 \mathbf{x}', \\ e_t &= \frac{1}{2} \int_V \rho(\mathbf{x}') G_\ell(\mathbf{x} - \mathbf{x}') d^3 \mathbf{x}' \int_V |\Delta \mathbf{u}_\ell(\mathbf{x}, \mathbf{x}')|^2 G_\ell(\mathbf{x} - \mathbf{x}') d^3 \mathbf{x}' \\ &\quad + \frac{1}{2} \int_V \Delta \rho_\ell(\mathbf{x}, \mathbf{x}') |\Delta \mathbf{u}_\ell(\mathbf{x}, \mathbf{x}')|^2 G_\ell(\mathbf{x} - \mathbf{x}') d^3 \mathbf{x}', \end{aligned} \quad (21)$$

where  $\Delta \rho_\ell(\mathbf{x}, \mathbf{x}') = \rho(\mathbf{x}') - \rho_\ell(\mathbf{x})$  and  $\Delta \mathbf{u}_\ell(\mathbf{x}, \mathbf{x}') = \mathbf{u}(\mathbf{x}') - \mathbf{u}_\ell(\mathbf{x})$ .

Figure 5 shows how various parts of the kinetic energy density depend on the smoothing length  $\ell$ . The behaviour of the volume averages of these contributions to the kinetic energies is much less straightforward than for magnetic energy, except for  $t > 1.45$  Gyr where similar monotonic dependence on  $\ell$  is observed. Additionally for both  $0.8 \leq t < 1.1$  Gyr and  $1.1 \leq t < 1.45$  Gyr, we observe that the fluctuating kinetic energy  $\langle e_{st} + e_t \rangle_V$  is equal to zero within errors for  $50 \leq \ell \leq 100$  pc. This results from cancellation between  $\langle e_{st} \rangle_V$  and  $\langle e_t \rangle_V$ , with  $\langle e_{st} \rangle_V$  significantly negative, as confirmed by figure 7. The quantity  $e_{st} = \langle u_i \rangle_\ell \mu(\rho, u_i)$  is dominated by the contribution of the  $z$ -component of the velocity field ( $i = 3$ ) since  $\langle u_z \rangle_\ell$  is much larger than the  $x$ - and  $y$ - components because of a systematic gas outflow from the midplane.



The gas involved in the outflow is hotter and less dense than on average, leading to large negative values of  $-\langle\rho\rangle_\ell\langle u_z\rangle_\ell$  for  $z > 0$  and, hence, of  $\langle u_z\rangle_\ell\mu(\rho, u_z) = \langle u_z\rangle_\ell(\langle\rho u_z\rangle_\ell - \langle\rho\rangle_\ell\langle u_z\rangle_\ell)$  (the dominant component of  $e_{st}$ ).

For  $z < 0$  kpc, the mean vertical velocity driven by the supernovae  $\langle u_z\rangle_\ell$  is large and negative, resulting in large, positive values of  $\mu(\rho, u_z) = \langle\rho u_z\rangle_\ell - \langle\rho\rangle_\ell\langle u_z\rangle_\ell$ . Thus, the opposite signs of  $\langle u_z\rangle_\ell$  and  $\mu(\rho, u_z)$  result in large, negative values of  $e_{st}$  for negative  $z$ . These large, negative values for  $e_{st}$  appear to dominate the kinetic energy statistics at earlier times. This is discussed in more detail below.

The variation with  $\ell$  of the fluctuating kinetic energy produces a more complicated pattern than for fluctuating magnetic energy, see figure 5. The values of  $\ell$  for which the variation is weak are  $\ell > 300$  pc. Such a smoothing length is much larger than any estimate of the correlation scale of the random motions, and the optimal smoothing lengths of both  $\rho$  or  $\mathbf{u}$ . As a result, the criterion that the variation of the fluctuating kinetic energy must be weak is not an appropriate method for choosing suitable smoothing lengths for either  $\rho$  or  $\mathbf{u}$ .

## 6. Influence of the mean-field dynamo

Figures 4 and 5 both suggest that the structures of magnetic and kinetic energy distributions vary with the state of the mean-field dynamo. We first examine the vertical structure of both energies, comparing the three temporal stages discussed previously, to demonstrate the changes in structure caused by the dynamo.

At early times, when the fluctuating magnetic field dominates the mean field, the magnetic field is strongest at  $z = 0$  kpc, but significant local maxima (in each of  $\langle e_B\rangle_\ell$ ,  $e_{B\ell}$  and  $e_b$ ) develop at  $|z| = 0.3$  kpc. This is in line with the kinetic energy, where  $\langle e_k\rangle_\ell$  is maximal at the midplane, but  $e_s$  and  $e_{st}$  have extrema at  $|z| = 0.3$  kpc; see figures 6a and 7a.

As the mean field dynamo saturates, the mean magnetic field dominates compared to the fluctuating field. The vertical profile of the smoothed total magnetic energy is increasingly dominated by the mean magnetic energy, with the peaks at  $|z| = 0.3$  kpc now dominating; see figures 6b,c. The increasing mean magnetic field significantly alters the vertical profile of the kinetic energy, as shown in figures 7b,c. All the components in the division of kinetic energy are ultimately concentrated near the midplane (so that the peaks at  $z = 0.3$  kpc have been suppressed), and the maximum value of  $\langle e_k\rangle_\ell$  decreases.

Strong mean magnetic fields generated via dynamo action in the same ISM simulations have been shown to suppress outflows of the hot gas (see [Evirgen et al. 2017](#)), which are associated with high values of kinetic energy. This would lead to a vertical profile of kinetic energy with the characteristics present in figure 7c. The most dramatic change is the effect on the ‘intermediate scale’ component of the kinetic energy,  $e_{st}$ . As the magnetic field strength increases, the magnitude of the horizontal average of  $e_{st}$  decreases significantly, becoming small except near to the midplane. As a result, the kinetic energy is approximately split between the mean and small-scale energies  $e_s$  and  $e_t$ .

As this change appears to be the most significant, we focus on horizontal planes from the snapshots  $t = 0.8$  Gyr and  $t = 1.6$  Gyr at which the vertical profiles of  $e_{st}$  shown in figure 7 show the most profound differences.

In the kinematic stage of the mean-field dynamo, there are regions in which  $e_{st}$  differs from zero significantly, whilst  $\langle e_k\rangle_\ell$  is uniform by comparison (see figure 8). The mean and turbulent kinetic energies,  $e_s$  and  $e_t$  respectively (not shown here), are also significant in the same regions as  $e_{st}$ . The contribution to  $e_{st}$  from the  $z$ -component of  $\mathbf{u}$ ,  $\langle u_z\rangle_\ell\mu(\rho, u_z)$ , comprises a large fraction of the total kinetic energy (about 80%) and so the vertical flow is dominant in  $e_{st}$  at this stage. The values for which  $e_{st}$  is highest strongly coincide with regions of large positive  $\langle u_z\rangle_\ell$ , which are the regions of hot gas outflows. Thus, at the kinematic stage of the mean-field dynamo,  $e_{st}$  is strongly correlated with the outflows of hot gas. In this model, the mean magnetic field is absent from the regions of hot gas, as demonstrated by [Evirgen et al. \(2017\)](#). Thus, the mean magnetic field also avoids regions in which  $e_{st}$  is significant in magnitude.

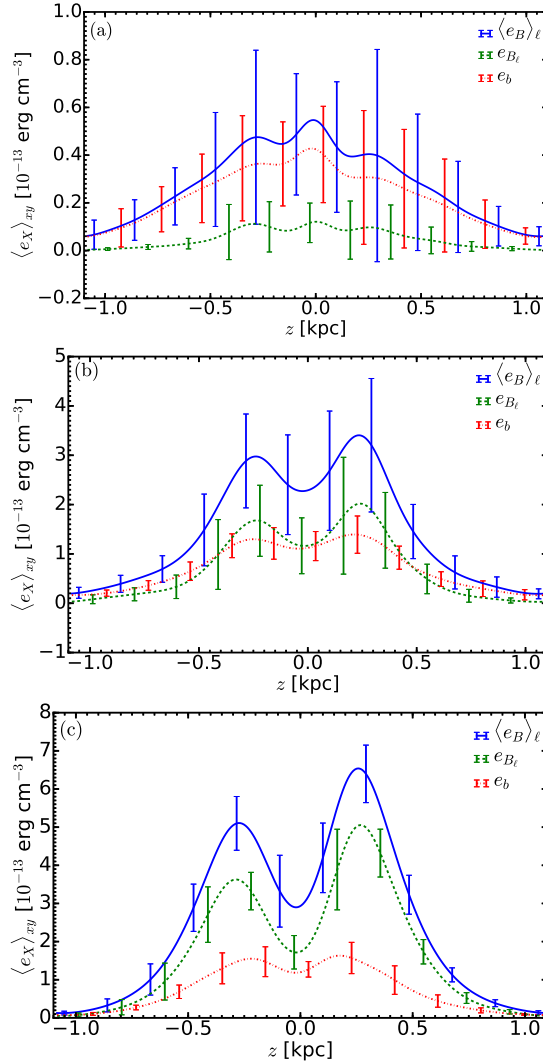


Figure 6. Vertical profiles of the horizontal averages of the smoothed total magnetic energy,  $\langle \langle e_B \rangle_\ell \rangle_{xy}$  (blue, solid), mean magnetic energy,  $\langle e_{B_\ell} \rangle_{xy}$  (green, dashed), and fluctuating magnetic energy,  $\langle e_b \rangle_{xy}$  (red, dash-dotted); at times (a)  $0.8 \leq t < 1.1$  Gyr, (b)  $1.1 \leq t < 1.45$  Gyr and (c)  $t \geq 1.45$  Gyr. The smoothing length applied for each snapshot is  $\ell = 75$  pc.

The effect of the amplified mean magnetic field on the kinetic energies is demonstrated in figure 9. The values of  $e_{st}$  are reduced significantly and  $e_{st}$  appears more uniform. By contrast,  $\langle e_k \rangle_\ell$  is now more significant and the non-uniform structure of  $\langle e_k \rangle_\ell$  is more pronounced. The contribution to  $e_{st}$  from the vertical flow is also dramatically reduced, and no longer dominates. The mean vertical velocity is reduced both in maximal value and in the size of regions in which  $\langle u_z \rangle_\ell$  is significant, indicative of the suppression of the hot gas outflow. Thus, the partial suppression of the hot gas outflow by the mean magnetic field has both significantly reduced the value of  $e_{st}$  and resulted in the dynamics of the overall kinetic energy becoming independent of the behaviour of  $e_{st}$ .

## 7. Comparison with horizontal averaging

To emphasise the physical relevance of the filtered quantities as representations of the mean and fluctuating fields, as compared with the corresponding quantities from horizontal averaging, in this section we perform a direct comparison.

Figure 10 shows a representative comparison of the two decompositions. In both panels, the solid blue curve gives the total vertical velocity at fixed  $y$  and  $z$ ; panel (a) also shows the fluctuating parts

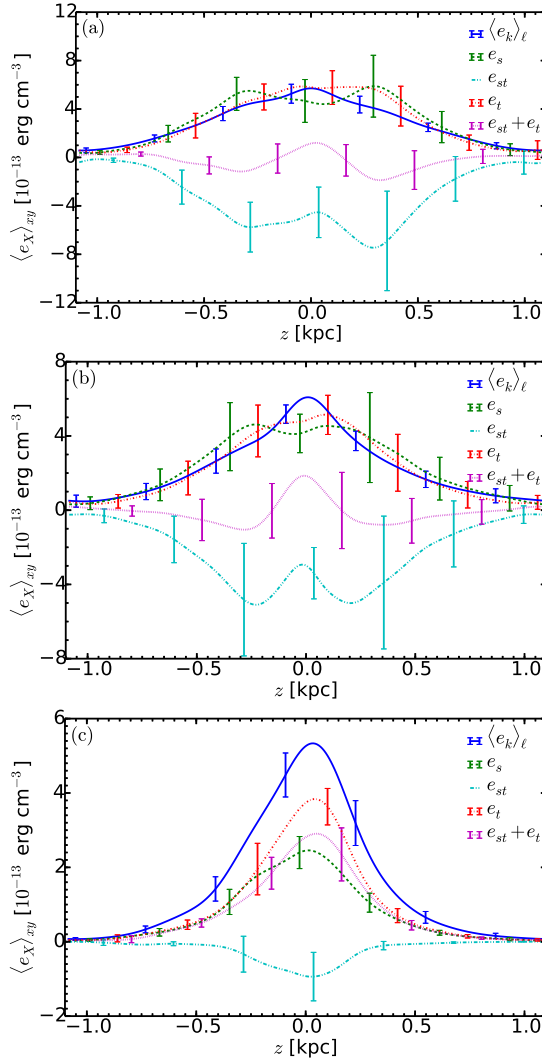


Figure 7. As in figure 6 but for the smoothed total kinetic energy density  $\langle\langle e_k \rangle\rangle_{xy}$  (blue, solid), mean kinetic energy density  $\langle e_s \rangle_{xy}$  (green, dashed), ‘intermediate scale’ kinetic energy density  $\langle e_{st} \rangle_{xy}$  (cyan, dash-dot-dotted), fluctuating kinetic energy density  $\langle e_t \rangle_{xy}$  (red, dot-dashed), and the sum,  $\langle e_{st} + e_t \rangle_{xy}$  (purple, dotted); at times (a)  $0.8 \leq t < 1.1$  Gyr, (b)  $1.1 \leq t < 1.45$  Gyr and (c)  $t \geq 1.45$  Gyr. As in figure 6, the smoothing length applied is  $\ell = 75$  pc.

obtained via both averaging methods, and panel (b) shows the corresponding mean parts. We notice that here the velocity is small in magnitude for  $x < 0$ . However, there is a region of higher vertical velocity for  $x > 0$ , which corresponds to gas flowing away from the midplane. This region has the typical characteristics of a hot gas structure.

Since horizontal averaging takes an average value for the entire horizontal plane, panel (b) shows the mean vertical gas velocity as constant with respect to  $x$ , with  $U_{h,z} = \langle u_z \rangle_{xy} \approx 20 \text{ km s}^{-1}$ . The systematic flow seen in  $x > 0$  kpc has approximate velocity  $60\text{--}80 \text{ km s}^{-1}$ . Consequently, the fluctuating field, derived using horizontal averaging, retains a large proportion of this systematic flow. This is apparent in the similarity of the curves and magnitudes of the total vertical velocity and fluctuating vertical velocity defined using horizontal averaging. In general, where there are significant local deviations within a horizontal layer (as with the localised hot gas structures with large vertical velocity here), horizontal averaging will not capture the systematic features well. The horizontal mean calculated may be unrepresentative of the flow in most of the layer (as in panel (b)), and a significant proportion of the fluctuating part may simply be correcting for this locally inappropriate mean (as in panel (a)), rather than accurately reflecting local fluctuations. Here this leads to downwards fluctuating flows of up to  $20 \text{ km s}^{-1}$ ; in addition to inflating the magnitude of the fluctuating velocity, this

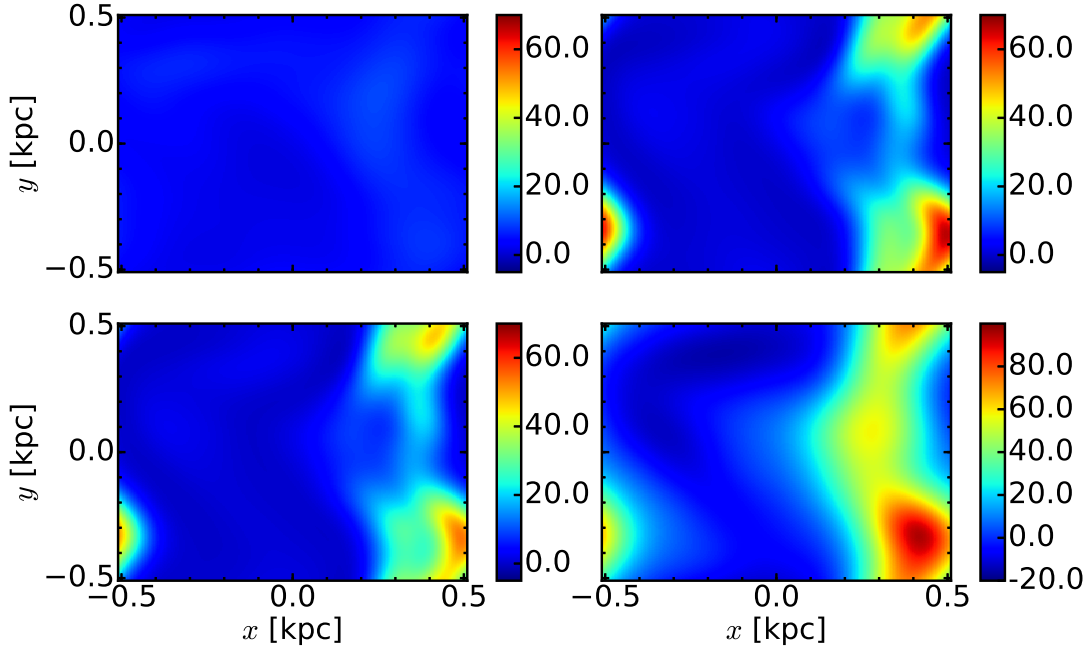


Figure 8. Horizontal slices of of the smoothed total kinetic energy density  $\langle e_k \rangle_\ell$  (top-left panel), the ‘intermediate-scale’ kinetic energy density  $e_{st}$  (top-right panel),  $\langle u_z \rangle_\ell \mu(\rho, u_z)$  the vertical contribution to  $e_{st}$  (bottom-left panel), all in units of  $10^{-13}$  erg  $\text{cm}^{-3}$ , and the mean vertical velocity  $\langle u_z \rangle_\ell$  (bottom-right panel) in  $\text{km s}^{-1}$ ; at  $z = 290$  pc from the snapshot  $t = 0.8$  Gyr. The smoothing length used is  $\ell = 75$  pc.

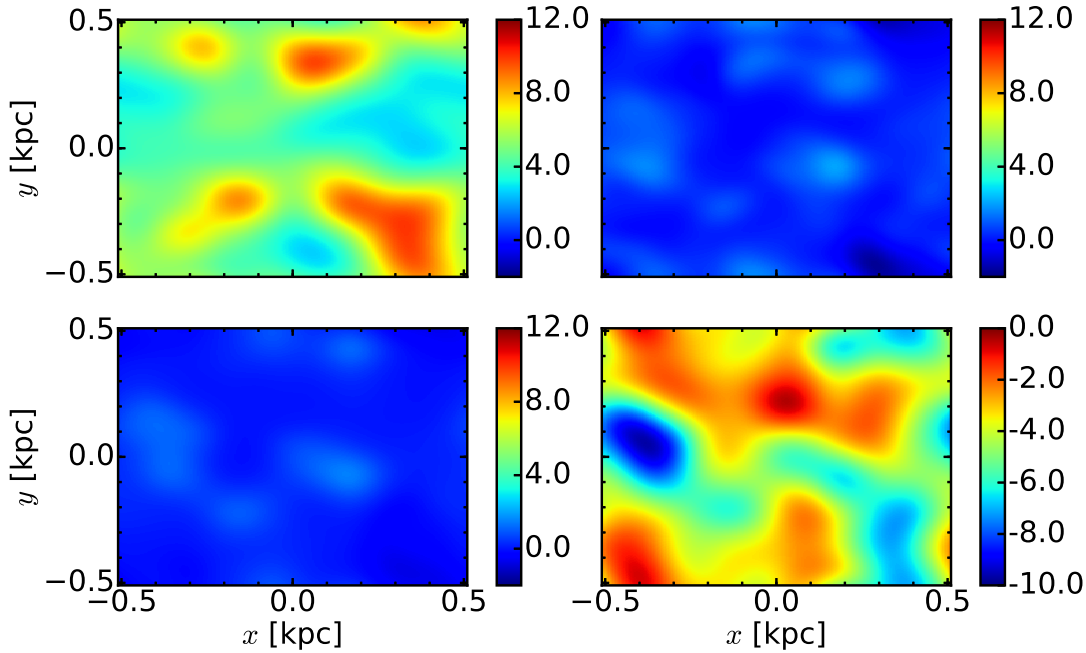


Figure 9. As in figure 8 but in the plane  $z = 30$  pc, at time  $t = 1.6$  Gyr.

misleadingly creates the impression of a systematic local flow towards the midplane.

By contrast, the mean vertical velocity obtained with Gaussian smoothing, shown by the dashed magenta curve of panel (b), extracts the systematic flow well, retaining information on the region of hot gas moving away from the plane. In addition, this mean retains features of the systematic vertical velocity more accurately in regions where that velocity is smaller (close to zero). The fluctuating vertical velocity derived using Gaussian smoothing retains a smaller proportion of the systematic background trend, so its magnitude remains commensurately small.

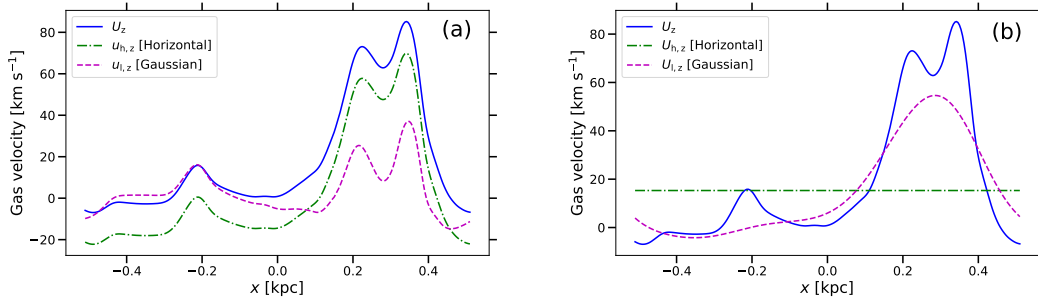


Figure 10. Vertical component of gas velocity as a function of  $x$  (galactocentric radius) at fixed  $y$  and  $z$ , to compare horizontal averaging and Gaussian smoothing. In Panel (a), we present the total vertical gas velocity  $U_z = u_z$  (blue solid); fluctuating vertical velocity defined using horizontal averaging (green dash dotted),  $u_{h,z} = u_z - \langle u_z \rangle_{xy}$ ; fluctuating vertical velocity defined using Gaussian smoothing (magenta dashed),  $u_{l,z} = u_z - \langle u_z \rangle_\ell$ . In Panel (b), we present the total vertical gas velocity (blue solid); mean vertical velocity defined using horizontal averaging (green dash dotted),  $U_{h,z} = \langle u_z \rangle_{xy}$ ; mean vertical velocity defined using Gaussian smoothing (magenta dashed),  $U_{l,z} = \langle u_z \rangle_\ell$ .

Given that the system discussed here, like many other astrophysical systems, contains systematic features such as those discussed above — driven by the bubbles of hot gas associated with the SN activity in the case of the ISM, which are well-defined local 3D features that cannot be well represented by a horizontal average across the whole layer — it is perhaps not surprising that Gaussian smoothing extracts such systematic features more successfully than horizontal averaging. This will also be true in many other instances with pronounced local 3D structures. (It should be noted that the effect will not be so pronounced where the horizontal layer is large enough to contain multiple such structures — involving both outflows and inflows — which might then average out over the full layer. But even in such cases, the horizontally-averaged mean cannot capture these systematic features, which should sensibly be characterised as part of the large-scale field, rather than as fluctuations.)

Gaussian smoothing (or filtering with any other kernel) is not technically or conceptually more difficult to implement and interpret than any other averaging method, but it requires an appropriate filtering scale to be identified. The Gaussian kernel used here is isotropic but the filtering approach also offers the opportunity to use anisotropic kernels wherever appropriate. This can be specially important in the case of the velocity field; for example, SN remnants expand more strongly along the density gradient in galactic discs, and the hot gas is buoyant. It is reasonable to expect that the magnetic field reflects such features of the gas flow and application of an anisotropic filtering kernel might lead to a clearer physical picture, although this would introduce an additional parameter, the degree of the kernel anisotropy. This situation is quite similar to that with the anisotropic wavelet decomposition (e.g., [Patrikeev et al. 2006](#)).

## 8. Discussion

We have applied Gaussian smoothing to obtain mean fields for magnetic field, density and velocity in a simulation of the multiphase interstellar gas: a complex, partially ordered magnetohydrodynamic system that supports the mean-field dynamo action. The optimal smoothing lengths were obtained by spectral analysis of each field independently. We find  $\ell = 75$  pc, approximately 19 grid cells, as an appropriate smoothing length to use for each of these fields. Such a result is likely to be sensitive to the choice of simulation parameters, and should be investigated with a subsequent detailed exploration of the parameter space. However, we have successfully demonstrated that an optimal value of  $\ell$  for each of the three fundamental physical fields is indeed possible in our simulation of the ISM. We have also shown that Gaussian smoothing, unlike horizontal averaging, retains large-scale 3D features of the mean fields. The filtering approach allows for a more physically-meaningful decomposition into mean and fluctuating parts for each variable and for their higher statistical moments, such as the magnetic and kinetic energy densities.



It is natural to expect that the magnetic, density and velocity fields can have distinct spatial structures since they are controlled by different physical processes, even though they do not evolve independently. The Gaussian smoothing successfully reveals such differences (e.g., the different quantities have different correlation lengths), as shown in [Hollins \*et al.\* \(2017\)](#) for a filtering length of 50 pc. (The change to 75 pc suggested here does not affect this significantly.) [Gressel and Elstner \(2020\)](#) apply kernel filtering to acquire the mean magnetic field from simulations of SN driven turbulence and explore the scale separation between mean and random fields in their simulations. They show that the diamagnetic transport of the mean field is stronger when the filtering scale is smaller.

We examine the mean and fluctuating magnetic and kinetic energies, using the generalised central moments to define the energy density of the fluctuations. We examine the dependencies of the energies on  $\ell$ , and on the magnetic dynamo saturation. This allows us to identify the key physical processes affecting the mean and fluctuating fields. Amplification of the mean magnetic field by dynamo action has a significant impact on the contributions to the magnetic and kinetic energies due to the mean fields, fluctuations and, in the case of the kinetic energy, advection of the fluctuations by the mean flow. The growing mean magnetic field shifts the maximum of the vertical profile of kinetic energy towards the disc midplane. part of the kinetic energy density associated with the advection of the velocity fluctuations by the mean flow,  $e_{st}$ , is closely correlated with a systematic gas outflow and is partly suppressed by the growing mean magnetic field. This results in a dramatic reduction in  $e_{st}$  at late times in the simulation, when the kinetic energy is mostly associated with the large-scale flow and the velocity fluctuations.

### Acknowledgement

The authors wish to acknowledge CSC–IT Center for Science, Finland, for computational resources Grand Challenge SNDYN. A.S., A.F., and G.R.S. were supported by the Leverhulme Trust Grant RPG-2014-427 and STFC Grant ST/N000900/1 (Project 2). F.A.G. acknowledges support from the Academy of Finland ReSoLVE Centre of Excellence (grant 307411) and Ministry of Education and Culture Global AI-Plasma Physics Pilot.

### References

- Aluie, H., Coarse-grained incompressible magnetohydrodynamics: analyzing the turbulent cascades. *New J. Phys.*, 2017, **19**, 025008.
- Armstrong, J.W., Rickett, B.J. and Spangler, S.R., Electron density power spectrum in the local interstellar medium. *Astrophys. J.*, 1995, **443**, 209–221.
- Bendre, A., Gressel, O. and Elstner, D., Dynamo saturation in direct simulations of the multi-phase turbulent interstellar medium. *Astron. Nachr.*, 2015, **336**, 991.
- Brandenburg, A., Korpi, M.J. and Mee, A.J., Thermal Instability in Shearing and Periodic Turbulence. *Astrophys. J.*, 2007, **654**, 945–954.
- Brandenburg, A. and Subramanian, K., Astrophysical magnetic fields and nonlinear dynamo theory. *Phys. Rep.*, 2005, **417**, 1–209.
- de Avillez, M.A. and Breitschwerdt, D., The Generation and Dissipation of Interstellar Turbulence: Results from Large-Scale High-Resolution Simulations. *Astrophys. J. Lett.*, 2007, **665**, L35–L38.
- de Avillez, M.A. and Breitschwerdt, D., The Diagnostic O VI Absorption Line in Diffuse Plasmas: Comparison of Non-equilibrium Ionization Structure Simulations to FUSE Data. *Astrophys. J. Lett.*, 2012a, **761**, L19.
- de Avillez, M.A. and Breitschwerdt, D., Time-dependent Cooling in Astrophysical Plasmas: The Non-equilibrium Ionization Structure of the Interstellar Medium and X-Ray Emission at Low Temperatures. *Astrophys. J. Lett.*, 2012b, **756**, L3.
- Dobbs, C.L. and Price, D.J., Magnetic fields and the dynamics of spiral galaxies. *Mon. Not. R. Astron. Soc.*, 2008, **383**, 497–512.
- Dobbs, C.L. and Pringle, J.E., Age distributions of star clusters in spiral and barred galaxies as a test for theories of spiral structure. *Mon. Not. R. Astron. Soc.*, 2010, **409**, 396–404.
- Elmegreen, B.G. and Scalo, J., Interstellar Turbulence I: Observations and Processes. *Ann. Rev. Astron. Astrophys.*, 2004, **42**, 211–273.
- Evirgen, C.C., Gent, F.A., Shukurov, A., Fletcher, A. and Bushby, P., The distribution of mean and fluctuating magnetic fields in the multiphase interstellar medium. *Mon. Not. R. Astron. Soc.*, 2017, **464**, L105–L109.

- Eyink, G.L., Local energy flux and the refined similarity hypothesis. *J. Statist. Phys.*, 1995, **78**, 335–351.
- Eyink, G.L., Turbulent General Magnetic Reconnection. *Astrophys. J.*, 2015, **807**, 137.
- Eyink, G.L., Review of the Onsager “ideal turbulence” theory. *ArXiv e-prints*, 2018.
- Federrath, C., Roman-Duval, J., Klessen, R.S., Schmidt, W. and Mac Low, M.M., Comparing the statistics of interstellar turbulence in simulations and observations. Solenoidal versus compressive turbulence forcing. *Astron. Astrophys.*, 2010, **512**, A81.
- Gent, F.A., Mac Low, M.M., Käpylä, M.J., Sarson, G.R. and Hollins, J.F., Modelling supernova-driven turbulence. *Geophysical and Astrophysical Fluid Dynamics*, 2020, **114**, 77–105.
- Gent, F.A., Shukurov, A., Fletcher, A., Sarson, G.R. and Mantere, M.J., The supernova-regulated ISM - I. The multiphase structure. *Mon. Not. R. Aston. Soc.*, 2013a, **432**, 1396–1423.
- Gent, F.A., Shukurov, A., Sarson, G.R., Fletcher, A. and Mantere, M.J., The supernova-regulated ISM - II. The mean magnetic field. *Mon. Not. R. Aston. Soc.*, 2013b, **430**, L40–L44.
- Gent, F.A., Mac Low, M.M., Käpylä, M.J. and Singh, N.K., Small-scale Dynamo in Supernova-driven Interstellar Turbulence. *Astrophys. J. Lett.*, 2021, **910**, L15.
- Germano, M., Turbulence – The filtering approach. *J. Fluid Mech.*, 1992, **238**, 325–336.
- Girichidis, P., Naab, T., Hanasz, M. and Walch, S., Cooler and smoother - the impact of cosmic rays on the phase structure of galactic outflows. *Mon. Not. R. Aston. Soc.*, 2018, **479**, 3042–3067.
- Girichidis, P., Naab, T., Walch, S., Hanasz, M., Mac Low, M.M., Ostriker, J.P., Gatto, A., Peters, T., Wunsch, R., Glover, S.C.O., Klessen, R.S., Clark, P.C. and Baczynski, C., Launching Cosmic-Ray-driven Outflows from the Magnetized Interstellar Medium. *Astrophys. J. Lett.*, 2016a, **816**, L19.
- Girichidis, P., Walch, S., Naab, T., Gatto, A., Wunsch, R., Glover, S.C.O., Klessen, R.S., Clark, P.C., Peters, T., Derigs, D. and Baczynski, C., The SILCC (SImlulating the LifeCycle of molecular Clouds) project - II. Dynamical evolution of the supernova-driven ISM and the launching of outflows. *Mon. Not. R. Aston. Soc.*, 2016b, **456**, 3432–3455.
- Gressel, O., Bendre, A. and Elstner, D., On the magnetic quenching of mean-field effects in supersonic interstellar turbulence. *Mon. Not. R. Aston. Soc.*, 2013, **429**, 967–972.
- Gressel, O., Elstner, D., Ziegler, U. and Rüdiger, G., Direct simulations of a supernova-driven galactic dynamo. *Astron. Astrophys.*, 2008, **486**, L35–L38.
- Gressel, O. and Elstner, D., On the spatial and temporal non-locality of dynamo mean-field effects in supersonic interstellar turbulence. *Mon. Not. R. Aston. Soc.*, 2020, **494**, 1180–1188.
- Hanasz, M., Wółtański, D. and Kowalik, K., Global Galactic Dynamo Driven by Cosmic Rays and Exploding Magnetized Stars. *Astrophys. J. Lett.*, 2009, **706**, L155–L159.
- Heitsch, F., Mac Low, M.M. and Klessen, R.S., Gravitational Collapse in Turbulent Molecular Clouds. II. Magnetohydrodynamical Turbulence. *Astrophys. J.*, 2001, **547**, 280–291.
- Hill, A.S., Jounge, M.R., Mac Low, M.M., Benjamin, R.A., Haffner, L.M., Klingenberg, C. and Waagan, K., Vertical Structure of a Supernova-driven Turbulent, Magnetized Interstellar Medium. *Astrophys. J.*, 2012, **750**, 104.
- Hollins, J.F., Sarson, G.R., Shukurov, A., Fletcher, A. and Gent, F.A., Supernova-regulated ISM. V. Space and Time Correlations. *Astrophys. J.*, 2017, **850**, 4.
- Jounge, M.K.R. and Mac Low, M.M., Turbulent Structure of a Stratified Supernova-driven Interstellar Medium. *Astrophys. J.*, 2006, **653**, 1266–1279.
- Klessen, R.S., Heitsch, F. and Mac Low, M.M., Gravitational Collapse in Turbulent Molecular Clouds. I. Gasdynamical Turbulence. *Astrophys. J.*, 2000, **535**, 887–906.
- Korpi, M.J., Brandenburg, A., Shukurov, A. and Tuominen, I., Evolution of a superbubble in a turbulent, multi-phased and magnetized ISM. *Astron. Astrophys.*, 1999, **350**, 230–239.
- Krause, F. and Rädler, K.H., *Mean-Field Magnetohydrodynamics and Dynamo Theory*, 1980 (Oxford: Pergamon Press).
- Kulesza-Żydzik, B., Kulpa-Dybeł, K., Otmianowska-Mazur, K., Kowal, G. and Soida, M., Formation of gaseous arms in barred galaxies with dynamically important magnetic field: 3D MHD simulations. *Astron. Astrophys.*, 2009, **498**, L21–L24.
- Mac Low, M.M. and Klessen, R.S., Control of star formation by supersonic turbulence. *Rev. Mod. Phys.*, 2004, **76**, 125–194.
- Meneveau, C., Germano identity-based subgrid-scale modeling: A brief survey of variations on a fertile theme. *Phys. Fluids*, 2012, **24**, 121301-121301-14.
- Moffatt, H.K., *Magnetic Field Generation in Electrically Conducting Fluids*, 1978 (Cambridge: Cambridge University Press).
- Monin, A.S. and Yaglom, A.M., *Statistical Fluid Mechanics: Mechanics of Turbulence. Vol. 1*, 2007a (Mineola, N.Y.: Dover).
- Monin, A.S. and Yaglom, A.M., *Statistical Fluid Mechanics: Mechanics of Turbulence. Vol. 2*, 2007b (Mineola, N.Y.: Dover).
- Pakmor, R., Gómez, F.A., Grand, R.J.J., Marinacci, F., Simpson, C.M., Springel, V., Campbell, D.J.R., Frenk, C.S., Guillet, T., Pfrommer, C. and White, S.D.M., Magnetic field formation in the Milky Way like disc galaxies of the Auriga project. *Mon. Not. R. Aston. Soc.*, 2017, **469**, 3185–3199.
- Pakmor, R., Pfrommer, C., Simpson, C.M. and Springel, V., Galactic Winds Driven by Isotropic and Anisotropic Cosmic-Ray Diffusion in Disk Galaxies. *Astrophys. J. Lett.*, 2016, **824**, L30.
- Panchev, S., *Random Functions and Turbulence*, 1971 (Oxford: Pergamon Press).
- Patrikeev, I., Fletcher, A., Stepanov, R., Beck, R., Berkhuijsen, E.M., Frick, P. and Horellou, C., Analysis of spiral arms using anisotropic wavelets: gas, dust and magnetic fields in M51. *Astron. Astrophys.*, 2006, **458**, 441–452.
- Pencil Code Collaboration, Brandenburg, A., Johansen, A., Bourdin, P., Dobler, W., Lyra, W., Rheinhardt, M., Bingert, S., Haugen, N., Mee, A., Gent, F., Babkovskaia, N., Yang, C.C., Heinemann, T., Dintrans, B., Mitra, D., Candelaresi, S., Warnecke, J., Käpylä, P., Schreiber, A., Chatterjee, P., Käpylä, M., Li, X.Y., Krüger, J., Aarnes, J., Sarson, G., Oishi, J.,

- Schober, J., Plasson, R., Sandin, C., Karchniwy, E., Rodrigues, L., Hubbard, A., Guerrero, G., Snodin, A., Losada, I., Pekkilä, J. and Qian, C., The Pencil Code, a modular MPI code for partial differential equations and particles: multipurpose and multiuser-maintained. *The Journal of Open Source Software*, 2021, **6**, 2807.
- Rieder, M. and Teysier, R., A small-scale dynamo in feedback-dominated galaxies as the origin of cosmic magnetic fields - I. The kinematic phase. *Mon. Not. R. Astron. Soc.*, 2016, **457**, 1722–1738.
- Rieder, M. and Teysier, R., A small-scale dynamo in feedback-dominated galaxies - II. The saturation phase and the final magnetic configuration. *Mon. Not. R. Astron. Soc.*, 2017, **471**, 2674–2686.
- Sánchez-Salcedo, F.J., Vázquez-Semadeni, E. and Gazol, A., The Nonlinear Development of the Thermal Instability in the Atomic Interstellar Medium and Its Interaction with Random Fluctuations. *Astrophys. J.*, 2002, **577**, 768–788.
- Sarazin, C.L. and White, III, R.E., Steady state cooling flow models for normal elliptical galaxies. *Astrophys. J.*, 1987, **320**, 32–48.
- Scalo, J. and Elmegreen, B.G., Interstellar Turbulence II: Implications and Effects. *Ann. Rev. Astron. Astrophys.*, 2004, **42**, 275–316.
- Shukurov, A., Sarson, G.R., Nordlund, A., Gudiksen, B. and Brandenburg, A., The effects of spiral arms on the multi-phase ISM. *Astrophys. Space Sci.*, 2004, **289**, 319–322.
- Simard, C., Charbonneau, P. and Dubé, C., Characterisation of the turbulent electromotive force and its magnetically-mediated quenching in a global EULAG-MHD simulation of solar convection. *Adv. Space Res.*, 2016, **58**, 1522–1537.
- Slyz, A.D., Kranz, T. and Rix, H.W., Exploring spiral galaxy potentials with hydrodynamical simulations. *Mon. Not. R. Astron. Soc.*, 2003, **346**, 1162–1178.
- Sokoloff, D., Shukurov, A. and Ruzmaikin, A., Asymptotic solution of the alpha-squared-dynamo problem. *Geophys. Astrophys. Fluid Dyn.*, 1983, **25**, 293–307.
- Tennekes, H. and Lumley, J.L., *First Course in Turbulence*, 1972 (Cambridge, Mass.: MIT Press).
- Walch, S., Girichidis, P., Naab, T., Gatto, A., Glover, S.C.O., Wünsch, R., Klessen, R.S., Clark, P.C., Peters, T., Derigs, D. and Baczynski, C., The SILCC (SIMulating the LifeCycle of molecular Clouds) project - I. Chemical evolution of the supernova-driven ISM. *Mon. Not. R. Astron. Soc.*, 2015, **454**, 238–268.
- Wolfire, M.G., Hollenbach, D., McKee, C.F., Tielens, A.G.G.M. and Bakes, E.L.O., The neutral atomic phases of the interstellar medium. *Astrophys. J.*, 1995, **443**, 152–168.
- Zeldovich, Y.B., Ruzmaikin, A.A. and Sokoloff, D.D., *Magnetic Fields in Astrophysics*, 1983 (New York: Gordon and Breach).

## Appendix A: Parameters of the numerical model

The model discussed here aims to reproduce the statistical properties of the random ISM. With the integral scale of random fluctuations in various physical variables of order 50 pc (Hollins *et al.* 2017), the computational domain that we use contains about 400 correlation cells in each horizontal slice, providing sufficient statistics to obtain useful results. Other simulations of comparable physical content (e.g., Hill *et al.* 2012, Bendre *et al.* 2015) have computational boxes of a similar horizontal size of 0.8–1 kpc. The next largest physically distinct objects are superbubbles, of order 0.5–1 kpc in size, and OB associations and spiral arms whose scale is of order 1–3 kpc; modelling these phenomena would require significantly larger computational domains (and the next generation of computational models) although some of their features can be captured with existing models (e.g., Shukurov *et al.* 2004, de Avillez and Breitschwerdt 2007).

The vertical size of the domain is largely controlled by its horizontal size. A vertical extent of about 1 kpc is insufficient to capture fountain flows and model the temperature distribution in the halo, which would require heights greater than 5 kpc (see Hill *et al.* 2012). However, our simulations are able to fulfil our purpose of capturing the physics of the ISM near the midplane, excluding fountain flows, without any artefacts from the periodic boundary conditions. As argued by Gent *et al.* (2013a), periodic boundary conditions in the horizontal planes affect the outflow speed significantly at altitudes exceeding the horizontal extent of the region. Furthermore, the diameter of supernova shells increases to 0.4–0.6 kpc at  $|z| \approx 1$  kpc. Therefore, results obtained at  $|z| \gtrsim 1$  kpc in a computational box of  $1 \times 1$  kpc<sup>2</sup> horizontally may be questionable. Results from recent simulations performed in computational boxes taller than 1 kpc are mostly reported only within a few kiloparsec from the midplane (e.g., Hill *et al.* 2012). The domain used in our simulations includes two scale heights of the warm neutral gas.

With the range of  $|z|$  limited to 1 kpc in our simulations, we have made special effort to ensure that the boundary conditions at the top and bottom of the domain do not introduce any apparent artefacts into numerical solutions, such as a boundary layer with a strong gradient in any of the physical vari-

ables (Appendix C of [Gent et al. 2013a](#)). The limited vertical extent of the box is the main limitation of our model, but it can only be sensibly increased together with its horizontal size.

The mass loss rate through the top and bottom boundaries is about  $10^{-3} M_{\odot} \text{ yr}^{-1}$ , so  $10^6 M_{\odot}$  is lost in 1 Gyr, as compared to the total gas mass of  $10^7 M_{\odot}$  in the computational domain. This mass loss would correspond to a realistic value of the total mass loss rate of  $1 M_{\odot} \text{ yr}^{-1}$  for a galactic disc of radius 15 kpc, assuming the Galaxy is in a steady state. Our open boundary conditions allow for inflow as well as outflow (albeit in a rather *ad hoc* manner), which mitigates mass loss through the boundaries. The mass loss, despite being only modest, was compensated by a continuous mass replenishment (in proportion to the local gas density, for minimal impact on the dynamics) to maintain an approximately constant gas mass throughout the simulations.

The numerical resolution of 4 pc that we use has been carefully selected to reproduce accurately the known expansion laws and approximate internal structure of an isolated supernova remnant, subject to radiative cooling processes, until its expansion slows down to match the ambient speed of sound (Appendix B of [Gent et al. 2013a](#)). Thus, we are confident that our simulations model reliably the associated energy injection into the diffuse ISM. Indeed, the intensity of random flows, of order  $10 \text{ km s}^{-1}$  in the warm gas and higher in the hot phase, is in full agreement with both observations and simulations at a higher resolution. This is also true of the scales of the random flows, fractional volumes of the ISM phases and other aspects of the modelled ISM. We have adjusted thermal conductivity so as to ensure that any structures produced by thermal instability are fully resolved at the 4 pc resolution. Comparable simulations of [de Avillez and Breitschwerdt \(2007, 2012a\)](#) have an adaptive mesh with the finest separation of 1.25 pc, whereas [Hill et al. \(2012\)](#) have a resolution of 2 pc, both representing an arguably modest improvement. [Gent et al. \(2021\)](#) have now demonstrated that the small-scale (fluctuation) dynamo solutions are convergent only for a resolution of 1 pc and better, so at 4 pc the small-scale dynamo is not sufficiently resolved. This does not undermine the validity of averaging procedures presented here, but may affect the optimal value of the filtering scale  $\ell$ . We were unable to identify any further differences in the relevant results of these simulations that might be a consequence of the difference in the numerical resolution.

Self-gravity is ignored in our simulations since we do not attempt to model the very cold molecular gas which is the component significantly affected by self-gravity. Simulations with higher resolution would be required to model the higher densities and the associated more intense thermal and gravitational instabilities.

## Appendix B: Integral forms of the central moments of the second and third order

The central second-order statistical moment representing the energy density of magnetic field fluctuations  $e_b$  under smoothing at a scale  $\ell$  with a kernel  $G_{\ell}(\mathbf{x} - \mathbf{x}')$ , with  $\int_V G_{\ell}(\mathbf{x} - \mathbf{x}') d\mathbf{x}' = 1$  and  $X_{\ell} \equiv \langle X \rangle_{\ell} = \int_V X(\mathbf{x}') G_{\ell}(\mathbf{x} - \mathbf{x}') d^3 \mathbf{x}'$  for a scalar or vectorial quantity  $X$ , is given by

$$\begin{aligned} 8\pi e_b &= 8\pi (\langle e_B \rangle_{\ell} - e_{B_{\ell}}) = \mu(b_i, b_i) = \langle \mathbf{B} \cdot \mathbf{B} \rangle_{\ell} - \langle \mathbf{B} \rangle_{\ell} \cdot \langle \mathbf{B} \rangle_{\ell} = \int_V B^2(\mathbf{x}') G_{\ell}(\mathbf{x} - \mathbf{x}') d^3 \mathbf{x}' - B_{\ell}^2(\mathbf{x}) \\ &= \int_V |\mathbf{B}(\mathbf{x}') - \mathbf{B}_{\ell}(\mathbf{x})|^2 G_{\ell}(\mathbf{x} - \mathbf{x}') d^3 \mathbf{x}' + 2 \int_V \mathbf{B}(\mathbf{x}') \cdot \mathbf{B}_{\ell}(\mathbf{x}) G_{\ell}(\mathbf{x} - \mathbf{x}') d^3 \mathbf{x}' - 2B_{\ell}^2 \\ &= \int_V |\mathbf{B}(\mathbf{x}') - \mathbf{B}_{\ell}(\mathbf{x})|^2 G_{\ell}(\mathbf{x} - \mathbf{x}') d^3 \mathbf{x}' . \end{aligned} \quad (\text{B.1})$$

In a compressible flow, fluctuations in kinetic energy density involve second-order statistical moments evaluated as follows:

$$\mu(\rho, \mathbf{u}) = \langle \rho \mathbf{u} \rangle_{\ell} - \rho_{\ell} \mathbf{u}_{\ell} = \int_V \rho(\mathbf{x}') \mathbf{u}(\mathbf{x}') G_{\ell}(\mathbf{x} - \mathbf{x}') d^3 \mathbf{x}' - \rho_{\ell}(\mathbf{x}) \mathbf{u}_{\ell}(\mathbf{x})$$

$$\begin{aligned}
&= \int_V [\rho(\mathbf{x}') \mathbf{u}(\mathbf{x}') - \rho_\ell(\mathbf{x}) \mathbf{u}_\ell(\mathbf{x})] G_\ell(\mathbf{x} - \mathbf{x}') d^3 \mathbf{x}' \\
&= \int_V \{[\rho(\mathbf{x}') - \rho_\ell(\mathbf{x})] [\mathbf{u}(\mathbf{x}') - \mathbf{u}_\ell(\mathbf{x})] + \rho(\mathbf{x}') \mathbf{u}_\ell(\mathbf{x}) + \rho_\ell(\mathbf{x}) \mathbf{u}(\mathbf{x}') - 2\rho_\ell(\mathbf{x}) \mathbf{u}_\ell(\mathbf{x})\} G_\ell(\mathbf{x} - \mathbf{x}') d^3 \mathbf{x}' \\
&= \int_V [\rho(\mathbf{x}') - \rho_\ell(\mathbf{x})] [\mathbf{u}(\mathbf{x}') - \mathbf{u}_\ell(\mathbf{x})] G_\ell(\mathbf{x} - \mathbf{x}') d^3 \mathbf{x}' + \mathbf{u}_\ell(\mathbf{x}) \rho_\ell(\mathbf{x}) + \rho_\ell(\mathbf{x}) \mathbf{u}_\ell(\mathbf{x}) - 2\rho_\ell(\mathbf{x}) \mathbf{u}_\ell(\mathbf{x}) \\
&= \int_V [\rho(\mathbf{x}') - \rho_\ell(\mathbf{x})] [\mathbf{u}(\mathbf{x}') - \mathbf{u}_\ell(\mathbf{x})] G_\ell(\mathbf{x} - \mathbf{x}') d^3 \mathbf{x}' . \tag{B.2}
\end{aligned}$$

Similarly to equation (B.1),

$$\mu(u_i, u_i) = \int_V |\mathbf{u}(\mathbf{x}') - \mathbf{u}_\ell(\mathbf{x})|^2 G_\ell(\mathbf{x} - \mathbf{x}') d^3 \mathbf{x}' . \tag{B.3}$$

The third-order moment that appears in the kinetic energy density follows as (summation over repeated indices is understood)

$$\begin{aligned}
\mu(\rho, u_i, u_i) &= \langle \rho u_i u_i \rangle_\ell - 2\langle u_i \rangle_\ell \mu(\rho, u_i) - \langle \rho \rangle_\ell \mu(u_i, u_i) - \langle \rho \rangle_\ell \langle u_i \rangle_\ell \langle u_i \rangle_\ell \\
&= \langle \rho u_i u_i \rangle_\ell - 2\langle u_i \rangle_\ell (\langle \rho u_i \rangle_\ell - \langle \rho \rangle_\ell \langle u_i \rangle_\ell) - \langle \rho \rangle_\ell (\langle u_i u_i \rangle_\ell - \langle u_i \rangle_\ell \langle u_i \rangle_\ell) - \langle \rho \rangle_\ell \langle u_i \rangle_\ell \langle u_i \rangle_\ell \\
&= \langle \rho u_i u_i \rangle_\ell - 2\langle u_i \rangle_\ell \langle \rho u_i \rangle_\ell - \langle \rho \rangle_\ell \langle u_i u_i \rangle_\ell + 2\langle \rho \rangle_\ell \langle u_i \rangle_\ell \langle u_i \rangle_\ell \\
&= \int_V [\rho(\mathbf{x}') u^2(\mathbf{x}') - 2\mathbf{u}_\ell(\mathbf{x}) \cdot \rho(\mathbf{x}') \mathbf{u}(\mathbf{x}') - \rho_\ell(\mathbf{x}) u^2(\mathbf{x}') + 2\rho_\ell(\mathbf{x}) u_\ell^2(\mathbf{x})] G_\ell(\mathbf{x} - \mathbf{x}') d^3 \mathbf{x}' \\
&= \int_V [\rho(\mathbf{x}') - \rho_\ell(\mathbf{x})] |\mathbf{u}(\mathbf{x}') - \mathbf{u}_\ell(\mathbf{x})|^2 G_\ell(\mathbf{x} - \mathbf{x}') d^3 \mathbf{x}' - u_\ell^2(\mathbf{x}) \int_V \rho(\mathbf{x}') G_\ell(\mathbf{x} - \mathbf{x}') d^3 \mathbf{x}' \\
&\quad - 2\rho_\ell(\mathbf{x}) \mathbf{u}_\ell(\mathbf{x}) \cdot \int_V \mathbf{u}(\mathbf{x}') G_\ell(\mathbf{x} - \mathbf{x}') d^3 \mathbf{x}' + 3\rho_\ell(\mathbf{x}) u_\ell^2(\mathbf{x}) \\
&= \int_V [\rho(\mathbf{x}') - \rho_\ell(\mathbf{x})] |\mathbf{u}(\mathbf{x}') - \mathbf{u}_\ell(\mathbf{x})|^2 G_\ell(\mathbf{x} - \mathbf{x}') d^3 \mathbf{x}' . \tag{B.4}
\end{aligned}$$